United States Environmental
Protection Agency

EPA REPORT NO. 550/9-82-345

Office of Noise Abatement
and Control
Washington, D.C. 20460

A UNIFIED SET OF MODELS

FOR TIRE/ROAD NOISE GENERATION

JULY 1981

TECHNICAL REPORT DATA
Please read Instructions on the reverse before completing $II. A-717$

1. REPORT NO.	2.	3. RECIPIENT'S ACCESSION NO.
550/9-82-345		

4. TITLE AND SUBTITLE	5. REPORT DATE
A Unified Set of Models for Tire/Road Noise Generation	July 1981
	6. PERFORMING ORGANIZATION CODE

7. AUTHOR(S)	8. PERFORMING ORGANIZATION REPORT NO.
Kenneth J. Plotkin, Eric Stusnick	WR 81-26

9. PERFORMING ORGANIZATION NAME AND ADDRESS	10. PROGRAM ELEMENT NO.
Wyle Laboratories / Wyle Research 2361 Jefferson Davis Highway, Suite PL-404 Arlington, Virginia 22202	11. CONTRACT/GRANT NO. 68-01-6243

12. SPONSORING AGENCY NAME AND ADDRESS	13. TYPE OF REPORT AND PERIOD COVERED
U.S. Environmental Protection Agency Office of Noise Abatement and Control 1921 Jefferson Davis Highway Arlington, Virginia 22202	Interim Task
	14. SPONSORING AGENCY CODE

15. SUPPLEMENTARY NOTES

16. ABSTRACT

    A set of theoretical models has been prepared which describes the noise generated by tire/road interaction. The mechanisms considered are air pumping and carcass vibration. The models begin with a set of thin shell equations describing the motion of the belt of a radial ply tire, as derived by Bohm ("Mechanisms of the Belted Tire", *Ingeniur-Archiv*, XXXV, 1966). Structural quantities required for these equations are derived from material properties of the tire. The rolling shape of a tire is computed from the steady-state limit of these equations. Air pumping (monopole radiation from tread voids) is calculated by assuming that tread elements move passively on the deformed tire. Vibrational response of the tire is treated by the full time-dependent shell equations. The force input at the tire/road interface is calculated on the basis of tread geometry and distribution of contact patch pressure. This input is physically equivalent to the impulse distribution models widely used in the tire industry for tread pitch randomization. Subsequent radiation of sound is calculated by a Raleigh integral.

    These models have been embodied into a unified set of computer programs. Using the programs, the effect on noise of various tire design variations is computed and discussed. Trends which lead to low noise design are identified. A series of experiments are planned which will test the validity of the models, and provide a basis for their refinement before final documentation and dissemination.

17.	KEY WORDS AND DOCUMENT ANALYSIS		
a. DESCRIPTORS		b. IDENTIFIERS/OPEN ENDED TERMS	c. COSATI Field/Group
Tire noise Air pumping Carcass vibration Road noise			

18. DISTRIBUTION STATEMENT	19. SECURITY CLASS (This Report)	21. NO. OF PAGES
Unlimited	UNCLASSIFIED	60
	20. SECURITY CLASS (This page)	22. PRICE
	UNCLASSIFIED	

EPA Form 2220-1 (9-73)

This report has been approved for general availability. The contents of this report reflect the views of the contractor, who is responsible for the facts and the accuracy of the data presented herein, and do not necessarily reflect the official views or policy of the EPA or the tire industry. This report does not constitute a standard, specification, or regulation.

TABLE OF CONTENTS

i

LIST OF SYMBOLS *

a	speed of sound in air
A	cross-sectional area of belt (Section 2.3), tread area function (Sections 4 and 5)
A_c	cross-sectional area of cords in belt
$A(\phi_0)$	function describing tread area (Sections 4 and 5)
A_n, B_n, C_n, D_n	coefficients of Fourier series describing tire shape
C_p	phase velocity in belt
d	tread depth
d_r, d_t	radial and tangential damping, per unit length
$\lvert det \rvert$	magnitude of determinant
E, F, G, H	coefficients of inverted matrix (Section 2)
E_R	elastic modulus of rubber
E_s	elastic modulus of steel
EA	extensional stiffness of tread and belts
EI	bending stiffness of tread and belts
$f(\phi_i - \phi)$	function defining radial displacement at ϕ due to unit force at ϕ_i.
$F(\phi)$	force associated with tread/road interface.
G	geometric amplification factor (Section 3)
$G(\vec{r} \mid \vec{r}')$	Green's function (Section 4)
G_R	shear modulus of rubber
h	distance from neutral surface of bending to center of tread
$H(\phi - \phi_i)$	unit step function (Section 4)
k_r, k_t	radial and tangential bedding coefficients (Section 2)
k_a, k_t	wave number in air and tire (Section 4)
l	tread pitch length

---

* Where the same symbol is used for several different items, the corresponding sections or equations are indicated.

l_b	tread block length
l_v	tread void length
n	circumferential mode number
N	number of belt plies
p	acoustic pressure
P_r, P_t	radial and tangential external pressures
$P_{rs}, P_{rc}, P_{ts}, P_{tc}$	sine and cosine integrals of P_r and P_t
P	point force (Section 2); average contact force pressure (Section 4)
Q	resonant Q factor; inverse of loss factor
$\vec{r}$	vector from source to receiver; $|\vec{r}| = r$
R	local radius of curvature
R_o	unperturbed radius of tire
s	circumferential distance coordinate, measured from contact patch edge
s_o	coordinate on pavement; see Equations (48) through (50)
S	surface area
t	time
t_b	thickness of belt ply
t_s	sidewall thickness
t_t	tread thickness
T_o	tension in belt due to inflation pressure
U	speed of tire
u_n	normal velocity
V	tread void volume
v, w	tangential and radial displacements of belt
w_b	width of belt
w_t	effective width of tread
w_v	width of tread void
W	amplitude of harmonic component of radial displacement w

v

x,y,z	Cartesian coordinates re: contact patch center
y_g	shape of tread groove
y_{gi}	shape of i'th groove in full tread pattern
z_s	pavement texture profile
Δz	average vertical compression of rubber
α	cord angle (Section 2.3)
$\alpha, \beta, \gamma, \delta, \epsilon$	matrix coefficients (Section 2.2)
$\delta(\phi - \phi_i)$	Dirac delta function (Sectin 4)
ϵ	flow blockage factor (Section 3)
ζ	load distribution due to pavement texture
η	damping coefficient
θ_o	angle between sidewall and belt; see Figure 7
κ	local belt curvature
κ_o	curvature of unperturbed belt $= 1/R_o$
μ	mass density (per unit length) of tread and belts
ρ	density of air
ϕ	circumferential coordinate
ϕ_o	circumferential coordinate fixed to tire; corresponds to ϕ at $t = 0$
$\Delta\phi$	angle re: contact patch center
$\Delta\phi_{cp}$	angle from center to edge of contact patch
ω	radial frequency
Ω	angular velocity of tire
$(\dot{\ })$	time derivative
$(\ )'$	spatial derivative; either $\partial/\partial\phi$ or $\partial/\partial s$

1.0 INTRODUCTION

The acoustic environment near high-speed roads is currently dominated by noise from heavy truck tires. At highway speeds of 55 mph, peak A-weighted passby levels associated with the tires of a 5-axle truck-trailer set are on the order of 85 dB.[1] This is 2 to 3 dB higher than the noise levels associated with the engine and driveline components of trucks in use before the promulgation of truck noise regulations,[2] and substantially higher than driveline noise levels of new trucks complying with current regulations. To achieve the full benefits of current and future truck noise regulations at highway speeds, it is necessary to reduce tire levels by about 10 dB, to the order of 75 dB for heavy trucks. This corresponds to a level of between 68 to 70 dB for a 2-axle truck as used in the SAE J57a[3] test procedure — the most commonly used procedure for measuring truck tire noise.

Heavy truck tires in common use today exhibit noise levels that range from 73 to 85 dB as measured under SAE J57a test conditions, with each tire exhibiting a range of 2 to 4 dB depending on pavement type and state of wear. If attention is limited to modern design, on-highway tires, i.e., those with radial ply and/or rib to moderately aggressive tread patterns, the noise level range is 73 to 80 dB. Thus there has been some useful reduction associated with tire evolution. It has been shown that, by choosing from tires available today, economically beneficial selections can be made with noise levels in the 73 to 75 dB range.[4] This effectively reduces the gap between typical levels of several years ago and the level of 70 dB noted above.

To a certain degree, the evolutionary quieting of tires has occurred fortuitously as a result of the trends toward radial-ply carcass construction and less aggressive tread patterns. The design of tires specifically for noise control has been limited to tread randomization to eliminate pure tones,[5] avoiding designs with pocket-tread voids, and the development of drastically different designs with significantly reduced road performance.[6] Much of the reduction has come from a cut-and-try approach, without a full understanding of the noise-generating mechanisms. This approach cannot be expected to meet specific noise reduction goals on a definite timetable.

The most practical method of reducing tire noise levels is to apply a fundamental understanding of the noise-generation mechanisms to design tire modifications. The results of recent research studies have provided a better understanding of noise mechanisms, to the point where analytical noise models can be related to overall tire parameters. In the present study, a set of analytic models has been prepared which place the major noise mechanisms in a unified format with tire structural properties. This unified format permits the inclusion of noise as one more parameter in tire design, and

provides for evaluation of trade-offs between noise and performance. The noise mechanisms considered are air pumping from tread voids and carcass vibration radiation. These are the mechanisms identified as dominant in a previous study performed for EPA, during which physical models were formulated.[7] These models have been extended and refined in the present study. The effects of pavement texture have been included.

The purpose of this report is to document the formulation of a set of noise models and to identify potential low-noise designs by exercising these models. The foundation for the noise models is a model for the dynamic behavior of a tire carcass. Limiting the scope to radial tires (expected to dominate the tire market in the future), a set of thin-shell equations developed by Bohm[8] has been used. These equations and their solutions are described in Section 2.0. Section 3.0 presents a model for air pumping. The air pumping model used here is based on the physical behavior identified in Reference 7, and treats the motion of tread elements on a carcass whose shape is governed by Bohm's equations. The vibrational excitation of a treaded tire on a paved surface, and subsequent radiation of sound, is treated in Section 4.0. The force input at the tire/road interface is governed by the tread geometry and interfacial pressure. Detailed variations due to road texture are handled by an adaptation of Nilsson's linear excitation model.[9] The adaptation utilized here includes the extended reaction of the carcass. The model presented here is physically consistent with the tread impulse models widely used for tread pattern randomization, but contains the important extension that it predicts the amplitude as well as the spectral characteristics of the vibration input. The most important radiating section of a radial tire has experimentally been shown to be the tread area immediately following the contact patch exit.[7,10] Over this range, Bohm's equations reduce to the elastic beam model successfully used by Eberhardt.[10] Accordingly, Eberhardt's radiation calculation is incorporated in the set of models. An investigation of low-noise designs is presented in Section 5.0.

Portions of the models identified above have been well validated; however, other parts have not been and there has not been a full "end-to-end" validation of any tire noise model. Accordingly, an experimental phase is incorporated in a later task of the current program. Specially designed tires will be utilized to validate the models and to test low-noise design concepts. The investigation of low-noise designs presented in Section 5.0 utilizes the noise models in their present form.

The noise models are of a level of complexity which requires computer implementation. Formal documentation before experimental validation would be premature. However, to provide an overview as to the nature and extent of the model system, a brief discussion of the computer implementation of the models is included in each appropriate section.

2.0 EQUATIONS OF MOTION OF A TIRE

2.1 Thin Shell Equations

The modern radial ply tire typically consists of one or two carcass plies whose cords run from bead to bead at an angle 90° to the circumferential direction* (running radially outward in the sidewall, hence the name) plus several belt plies, limited to the tread area, whose cords run at much smaller angles, typically between 15° to 25°. Some designs include a first ply belt at large cord angle to provide a transition, but the overall effect is common to all radial tires: a reinforced belt whose strength is primarily circumferential lying on a relatively flexible transverse carcass. The belt and the sidewall properties are substantially different, and their behavior (other than the constraint that they are connected at the shoulder) is independent. This is in contrast to bias-ply tires, where equal numbers of plies at oblique angles form a continuous structure with similar properties in the sidewall and tread areas. Following experimental evidence that the radial tire belt behaves as a ring on an elastic foundation, Bohm[8] derived the following set of linearized equations for the tangential and radial displacements of the belt:

$$\mu\left(\ddot{v} + 2\Omega(\dot{v}' + \dot{w}) + \Omega^2(v'' + 2w' - v)\right) - \frac{EA}{R_o^2}(v'' + w')$$

$$+ k_t v - d_t(v'\Omega + \dot{v}) = p_t(\varphi, t) \qquad (1a)$$

$$\mu\left(\ddot{w} + 2\Omega(\dot{w}' - \dot{v}) + \Omega^2\left(w'' - 2v' - (w + R_o)\right)\right)$$

$$+ \frac{EA}{R_o^2}(v' + w) + \frac{EI}{R_o^4}(w^{iv} + 2w'' + w) - \frac{T_o}{R_o^2}(w + w'') \qquad (1b)$$

$$+ k_r w + d_r(w'\Omega + \dot{w}) = p_r(\varphi, t)$$

Figure 1 shows the coordinate system used. A complete list of symbols is presented at the beginning of this report. A note on the nomenclature of the belt stiffnesses is in order. Equations (1) are written as if for a homogeneous shell with elasticity E, cross-sectional area A and moment of inertia I. A tire is a heterogeneous structure. To avoid confusion between component material properties and quantities in Equations (1), the quantities EA and EI will each be treated as single entities, the extensional and bending stiffnesses, respectively.

---

* Cord angles in a tire are measured relative to the circumferential direction. This convention is used in this report. Additionally, angles may be cited as values from 0° to 90° with a left or right lay. The sense of the lay follows the same convention as the sense of a screw thread.
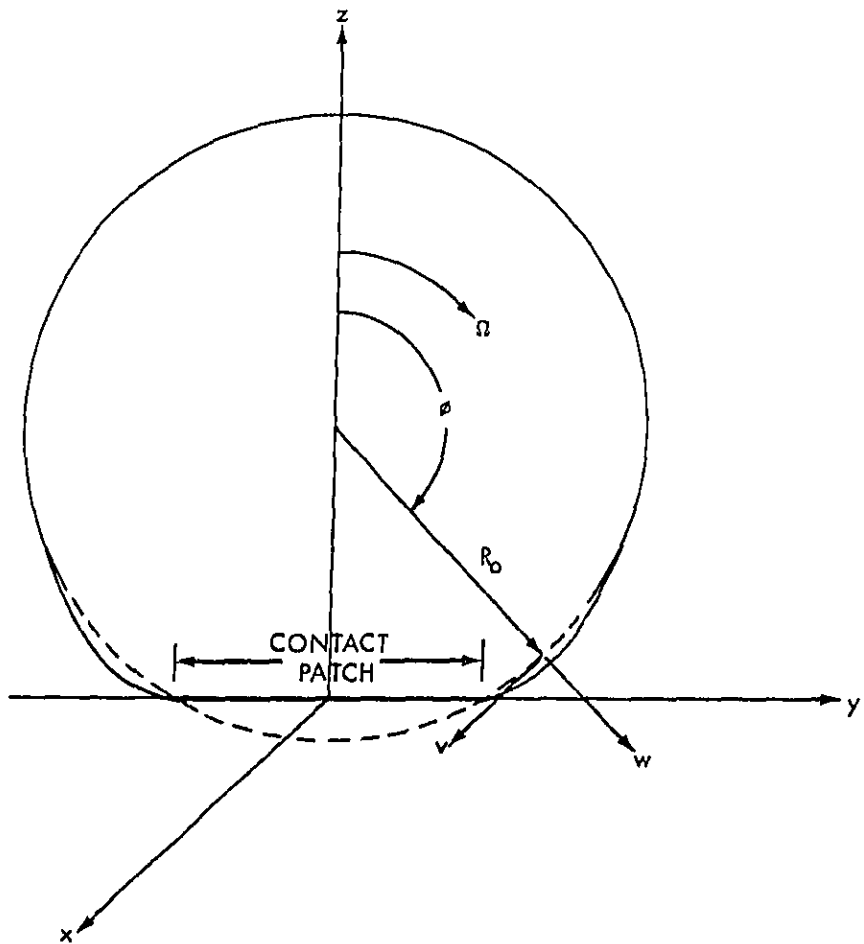
Figure I. Coordinate System.

Equations (1) are two-dimensional thin shell equations. They include membrane stresses, bending stresses, and radial and tangential momentum. The shell rests on an elastic damped medium whose radial and tangential stiffness and damping are given by k_r, k_t and d_r, d_t, respectively. Initial tension, T_o, is due to inflation pressure. The tire is spinning, so that the inertia terms include Coriolis and centripital components. The displacements v and w are in an Eulerian frame (i.e., as seen by an observer translating but not rotating with the tire) so that substantial derivatives appear in place of time derivative, e.g., d_r ($\dot{w}$ + $\Omega w'$) rather than $d_r \dot{w}$ for the radial damping.

In the present study, two limits of Equations (1) are of interest:

1. The steady state, which gives the stationary shape of a moving tire under load. This is the initial point about which noise generation is a perturbation.

2. The vibratory motion at high frequencies, corresponding to the audio frequency range.

The high-frequency vibration is addressed in Section 4.0. The remainder of this section treats the calculation of the stationary shape of a tire.

2.2 Stationary Shape of a Tire

Setting all time derivatives equal to zero, Equations (1) become

$$\left(\frac{EA}{R_o^2} - \mu\Omega^2\right) v'' - d_t \quad \Omega v' + (\mu\Omega^2 - k_t) v$$

$$+ \left(\frac{EA}{R_o^2} - 2\mu\Omega^2\right) w' = -p_t(\phi) \tag{2a}$$

$$\frac{EI}{R^4} w^{iv} + 2\left(\frac{EI}{R^4} + \mu\Omega^2 - \frac{T_o}{R_o^2}\right) w'' + (d_r \Omega) w'$$

$$+ \left(\frac{EA}{R_o^2} + \frac{EI}{R_o^4} - \frac{T_o}{R_o^2} + k_r - \mu\Omega^2\right) w - (\mu\Omega^2) R_o \tag{2b}$$

$$+ \left(\frac{EA}{R_o^2} - 2\mu\Omega^2\right) v' = p_r(\phi)$$

The equations have been reordered so as to group similar orders of derivative together.

2-3

Since Equations (2) are a linear system over a closed circumference, it is natural to seek solutions of the form

$$v = \sum_{n=0}^{\infty} (A_n \sin n\varphi + B_n \cos n\varphi)$$

(3)

$$w = \sum_{n=0}^{\infty} (C_n \sin n\varphi + D_n \cos n\varphi)$$

The method of solution is to substitute Equations (3) into (2), multiply each equation by $\sin m\varphi$ or $\cos m\varphi$, then integrate over one circumference. Noting the orthogonality of the harmonic functions, the following are obtained for the sine and cosine integrations of each equation for $n \geq 1$:

$$\left[\left(\frac{EA}{R_o^2} - \mu\Omega^2\right) n^2 + (k_t - \mu\Omega^2)\right] A_n - d_t \Omega n B_n$$

$$+ \left(\frac{EA}{R_o^2} - 2\mu\Omega^2\right) n D_n = \frac{1}{\pi} \int_0^{2\pi} P_t \sin n\varphi \, d\varphi$$

(4a)

$$d_t \Omega n A_n + \left[\left(\frac{EA}{R_o^2} - \mu\Omega^2\right) n^2 + (k_t - \mu\Omega^2)\right] B_n$$

(4b)

$$- \left(\frac{EA}{R_o^2} - 2\mu\Omega^2\right) n C_n = \frac{1}{\pi} \int_0^{2\pi} P_t \cos n\varphi \, d\varphi$$

$$- \left(\frac{EA}{R_o^2} - 2\mu\Omega^2\right) n B_n + \left[\frac{EI}{R_o^4} n^4 - \left(\frac{2EI}{R_o^4} + \mu\Omega^2 - \frac{T_o}{R_o^2}\right) n^2\right.$$

$$\left. + \left(\frac{EA}{R_o^2} + \frac{EI}{R_o^4} - \frac{T_o}{R_o^2} - \mu\Omega^2 + k_r\right)\right] C_n$$

(4c)

$$- d_r \Omega n D_n = \frac{1}{\pi} \int_0^{2\pi} P_r \sin n\varphi \, d\varphi$$

$$\left(\frac{EA}{R_o^2} - 2\mu\Omega^2\right) n\, A_n + d_r\, \Omega n\, C_n + \left[\frac{EI}{R_o^4} n^4 - \left(\frac{2EI}{R_o^4} + \mu\Omega^2 - \frac{T_o}{R_o^2}\right) n^2 \right.$$

$$\left. + \left(\frac{EA}{R_o^2} + \frac{EI}{R_o^4} - \frac{T_o}{R_o^2} - \mu\Omega^2 + k_r\right)\right] D_n = \frac{1}{\pi}\int_o^{2\pi} p_r \cos n\varphi\, d\varphi \tag{4d}$$

The following are obtained for the cosine integrals when $n = 0$:

$$\left(k_t - \mu\Omega^2\right) B_o = \frac{1}{2\pi}\int_o^{2\pi} p_t\, d\varphi \tag{5a}$$

$$\left(\frac{EA}{R_o^2} + \frac{EI}{R_o^4} - \frac{T_o}{R_o^2} - \mu\Omega^2 + k_r\right) D_o = \mu\Omega^2 R_o + \frac{1}{2\pi}\int_o^{2\pi} p_r\, d\varphi \tag{5b}$$

Equations (4) may be written in matrix form:

$$\begin{bmatrix} \alpha & -\beta & 0 & \gamma \\ \beta & \alpha & -\gamma & 0 \\ 0 & -\gamma & \delta & -\epsilon \\ \gamma & 0 & \epsilon & \delta \end{bmatrix} \cdot \begin{bmatrix} A_n \\ B_n \\ C_n \\ D_n \end{bmatrix} = \begin{bmatrix} p_{ts} \\ p_{tc} \\ p_{rs} \\ p_{rc} \end{bmatrix} \tag{6}$$

where α, β, γ, δ, ϵ are defined in Table I and correspond to the coefficients seen in Equations (4), and p_{ts}, etc., denote the integrals $(1/\pi)\int_0^{2\pi} p_t \sin n\varphi\, d\varphi$, etc. Note that these quantities are all functions of n. Equation (6) may be inverted to give the coefficients:

$$\begin{bmatrix} A_n \\ B_n \\ C_n \\ D_n \end{bmatrix} = \frac{1}{|\det|} \begin{bmatrix} E & F & G & H \\ -F & E & -H & G \\ -G & -H & I & J \\ H & G & -J & I \end{bmatrix} \cdot \begin{bmatrix} p_{ts} \\ p_{tc} \\ p_{rc} \\ p_{rc} \end{bmatrix} \tag{7}$$

where $E = \alpha(\delta^2 + \epsilon^2) - \delta\gamma^2$

$F = \beta(\delta^2 + \epsilon^2) + \epsilon\gamma^2$

2-5

Table I

Matrix Coefficients For Equation (6)

$$\alpha = \left(\frac{EA}{R_o^2} - \mu\Omega^2\right) n^2 + (k_t - \mu\Omega^2)$$

$$\beta = d_t \Omega n$$

$$\gamma = \left(\frac{EA}{R_o^2} - 2\mu\Omega^2\right) n$$

$$\delta = \frac{EI}{R_o^4} n^4 - \left(\frac{2EI}{R_o^4} + \mu\Omega^2 - \frac{T_o}{R_o^2}\right) n^2$$

$$+ \left(\frac{EA}{R_o^2} + \frac{EI}{R_o^4} - \frac{T_o}{R_o^2} - \mu\Omega^2 + k_r\right)$$

$$\epsilon = d_r \Omega n$$

$$G = (\beta\delta + \alpha\epsilon)\gamma$$

$$H = (\gamma^2 - \alpha\delta + \beta\epsilon)\gamma$$

$$I = \delta(\alpha^2 + \beta^2) - \alpha\gamma^2$$

$$J = \epsilon(\alpha^2 + \beta^2) + \beta\gamma^2$$

$$|det| = (\alpha^2 + \beta^2)(\delta^2 + \epsilon^2) + 2\gamma^2(\beta\epsilon - \alpha\delta) + \gamma^4$$

Provided $|det| \neq 0$, Equations (5) and (7) give explicit solutions for the coefficients as a function of external pressure p_r and p_t.

The possibility of $|det| = 0$ is of interest. The expression for $|det|$ may be rearranged as

$$|det| = (\alpha\delta - \gamma^2)^2 + \beta^2\delta^2 + \alpha^2\epsilon^2 + \beta^2\epsilon^2 + 2\gamma^2\beta\epsilon \qquad (8)$$

Noting that $\beta = d_t\,\Omega n$, $\epsilon = d_r\Omega n$, and that d_t and d_r cannot be negative, $|det|$ must always be positive when there is damping. The minimum value of $|det|$ occurs when $(\alpha\delta - \gamma^2) = 0$; this corresponds to the presence of standing waves. Standing waves occur at higher speeds than are of interest here. Previous calculations of standing waves from Bohm's equations, e.g., References 8 and 11, have shown good agreement with experiment.

Equations (5) and (7) provide an explicit solution for a given pressure distribution. However, the known boundary conditions for a rolling tire are that the tire is flat against the road within the contact patch, and $p_r = p_t = 0$ outside the contact patch. The solution is no longer explicit, and in fact is not unique since the tangential pressure depends on details of the tread/road frictional interaction which have not been considered. These difficulties have been handled in the present study by (a) assuming an explicit relation between p_t and p_r to resolve the indeterminacy, and (b) using an interative scheme to obtain a flat surface in the contact patch.

Published data[12] show that the tire/road interfacial pressures are approximately as sketched in Figure 2. The radial pressure is roughly uniform, with a slight bias toward the leading edge and some transition to zero at the edges. The tangential pressure exhibits a linear variation through the central part of the contact patch, with peak values corresponding to the vertical pressure times the coefficient of friction of the tread/road interface. A first approximation of the tangential pressure would be a ramp times the radial pressure:

$$p_t(\phi) = \frac{\Delta\phi}{\Delta\phi_{cp}}\ p_r(\phi), \quad -\Delta\phi_{cp} \leq \Delta\phi \leq \Delta\phi_{cp} \qquad (9)$$

where $\Delta\phi$ is measured from the center of the contact patch.

P_t

a) Tangential Pressure

TRAVEL DIRECTION

Shoulder Rib

Intermediate Rib

Center Rib

P_r

|←——CONTACT PATCH——→|
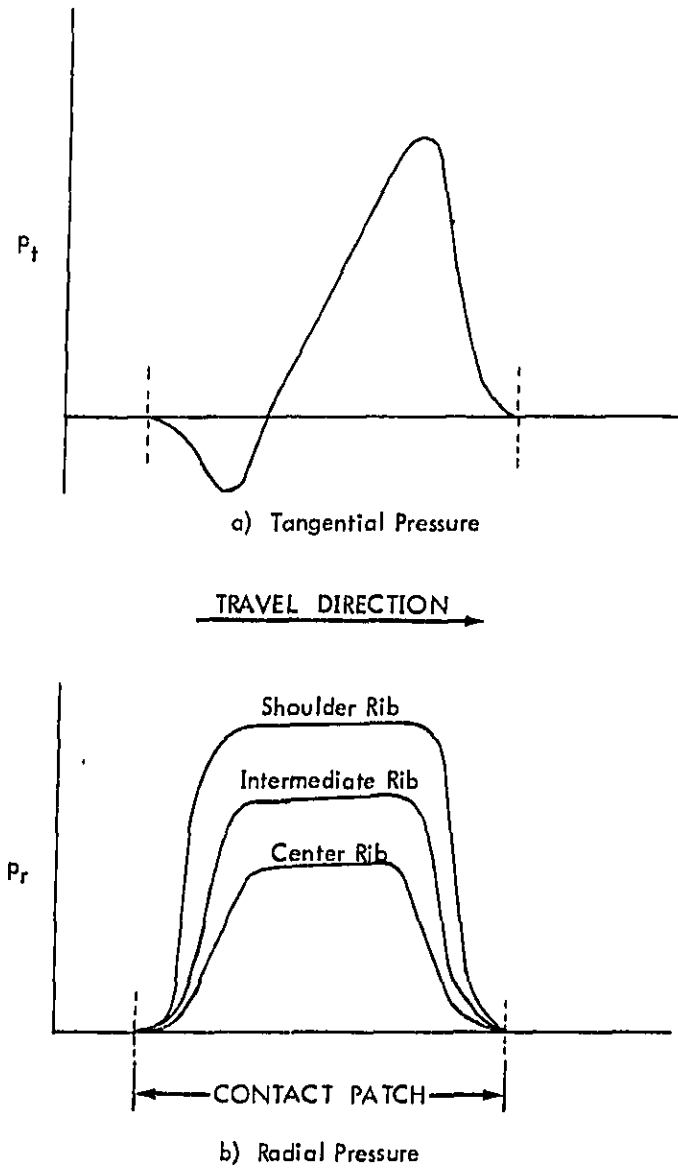
b) Radial Pressure

Figure 2. Typical Interfacial Radial and Tangential Pressures[12] Acting on a Point on the Tire as it Passes Through the Contact Patch.

2-8

In Sections 3.0 and 4.0, it is shown that noise generation depends primarily on radial motion w. It is also found, through examination of the matrix elements G, H, I, J in Equation (7), that p_t has an influence on w which is one to two orders of magnitude less than that of p_r. Accordingly, Equation (9) has been adopted to approximate p_t.

An iterative method is used to satisfy the flatness condition in the contact patch. The calculation is to some degree an inverse one, with contact patch length being the input variable. The procedure consists of the following steps:

1. An initial p_r is taken to be equal to the inflation pressure within the contact patch, and zero outside it.

2. The tire shape is computed from p_r.

3. The horizontal ground plane is placed such that it intersects the lower of the leading or trailing edge of the contact patch. The vertical height z of the tire is computed at each point within the contact patch.

4. The pressure p_r is adjusted proportionally to $-z$ at each point.

5. Steps 2, 3, and 4 are repeated, with the adjusted p_r, until flatness is achieved within some desired tolerance.

The proportionality between z and the increment to p_r at each point is based on the calculated shape due to a point load. Consider a point load P acting at ϕ_1. p_r is given by

$$p_r = P \delta (\phi - \phi_1) \tag{10}$$

where $\delta(\phi - \phi_1)$ is the Dirac delta function. The sine and cosine integrals of p_r (right-hand side of Equations (4) and (6)) are

$$p_{rs} = \frac{P}{\pi} \sin n \ (\phi_1) \tag{11}$$

$$p_{rc} = \frac{P}{\pi} \cos n \ (\phi_1)$$

Calculating C_n and D_n from Equation (7), then substituting into Equation (3), it is found that the radial displacement is given by

$$w(\phi) = P f (\phi_1 - \phi) \tag{12}$$

where

$$f (\phi_1 - \phi) = \frac{1}{\pi |det|} \sum \left[I_n \cos n \ (\phi_1 - \phi) + J_n \sin n \ (\phi_1 - \phi) \right] \tag{13}$$

The $n = 0$ term, D_o, has been left out of this analysis. It is small, and is also a constant value which is ultimately eliminated in this calculation of shape changes.

Figure 3 shows $f(\varphi_1 - \varphi)$ for a tire whose shape is calculated in Section 2.4. The curve is plotted over a φ range equal to plus and minus the contact patch length. There is a well-defined peak at the maximum at $\varphi = \varphi_1$. The values of f at the extrema of φ shown are not small compared to the value at $\varphi = \varphi_1$; the extended reaction of the tire must be considered when performing the adjustment in Step 4 above. If only one point were considered, the appropriate pressure adjustment would be

$$\Delta p = -z/(f(0) \Delta x) \tag{14}$$

where Δx is the mesh step size used in the pressure integrations. For an extended pressure distribution, using Equation (14) at each point would give much too large an adjustment. The procedure adopted is first to calculate Δp, from Equation (14), then divide it by the total mesh size. This provides an estimate for the first iteration. The adjustment for the second iteration can be more precisely estimated by comparing z from the initial step and the first iteration. This procedure was adopted, and was found to converge within two or three iterations. A rapid convergence is highly desirable for this calculation, due to considerations of computer time and cumulative rounding errors.

2.3 Structural Properties of a Tire

The equations of motion presented in Sections 2.1 and 2.2 are written in terms of structural properties of a uniform shell on a uniform elastic foundation. To apply these equations to a tire, it is necessary to compute equivalent properties for a real tire. Bohrn[8] derived the relationship between tire structure and effective properties for a radial tire. Several other authors, for example References 13 through 17, have derived structural parameters with emphasis on the detailed behavior of the cord/rubber composites which form the basic structure.

Figure 4 is a simplified sketch of a cross-section of a radial tire. A single 90° ply runs from bead to bead. When inflated, the carcass ply is approximately circular in the sidewall area. Several belt plies lie on the carcass ply in the tread area. They constrain the carcass, making it flatter across the crown. Not shown in this sketch are sidewall rubber, inner liner, cushions, etc.; these are secondary to the simplified structural model considered here.

The mass density μ follows directly from the cross-sectional area of the tread and belt area together with density of the materials. The remaining structural parameters require a more detailed analysis of the tire structure. Their derivations are discussed in the following subsections.

2-10
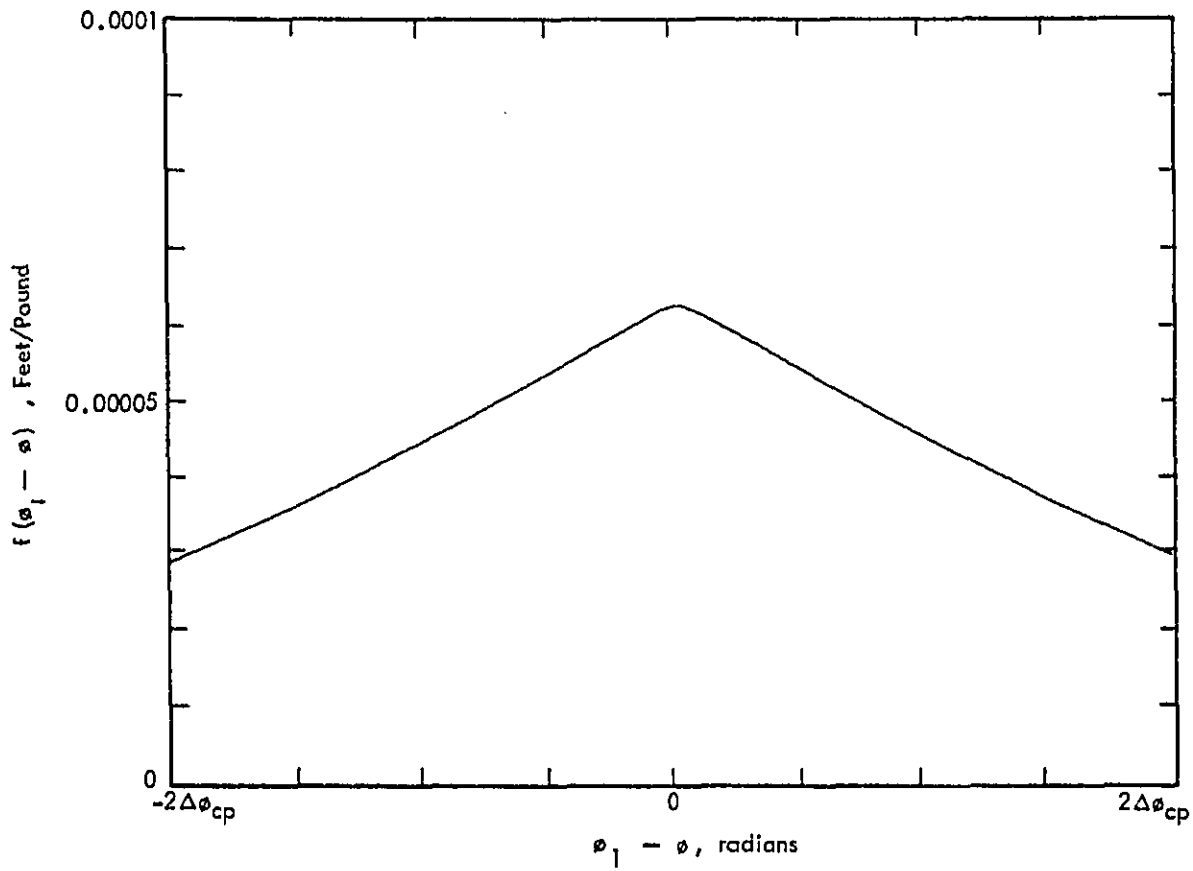
Figure 3. Function $f(\phi_1 - \phi)$ Defining Tire Response to a Point Load, Tire A.

2-11
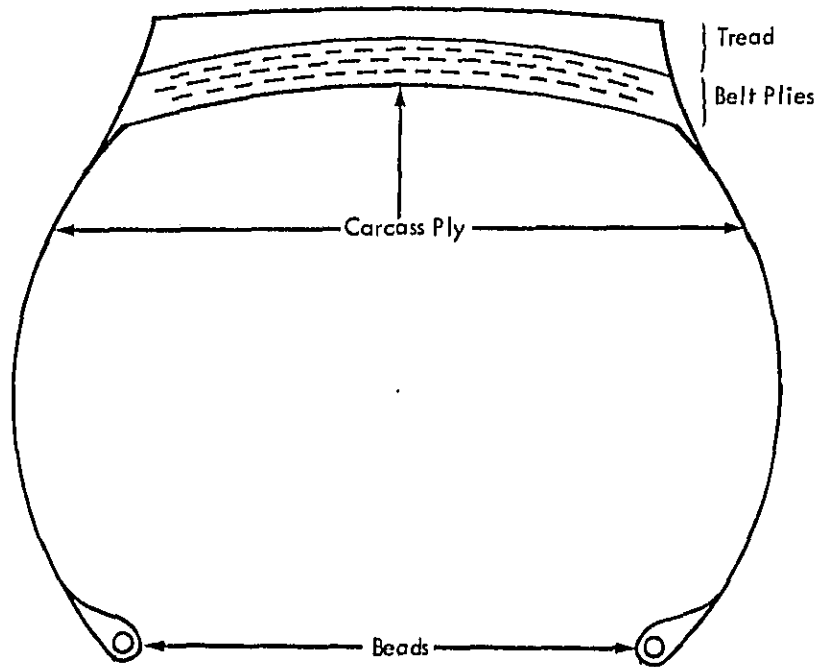
Figure 4. Simplified Sketch of Radial Tire Construction.

2.3.1 Extensional Stiffness

The extensional stiffness, EA, is based on the longitudinal properties of the tread belt. Figure 5 is a sketch of a single ply with cord angle α. The behavior of a single unconstrained ply under tension is quite complex, exhibiting asymmetric shears and twisting. If it is noted that plies are stacked with some degree of alternation of angle, and out-of-plane strains are constrained by the remainder of the tire, then it is reasonable to calculate longitudinal stiffness with the assumption of no shear in the circumferential and transverse directions, and with no twist. For steel cords of number and area such that the stiffness aligned with the cords is dominated by the steel, Bohm[8] and Posfalvi[17] obtain expressions which may be reduced to the following:

$$EA = 4(A - A_c) G_R (1 - \cot^2\alpha + \cot^4\alpha) \tag{15}$$

where A and A_c are the cross-sectional areas of the tread/belt construction and the cords, respectively, and G_R is the shear modulus of rubber. A Poisson's ratio of 1/2, typical for rubber, has been included.

Equation (15) corresponds to strain of the cords being negligible as compared to strain of the rubber. It is not applicable to very small α, but is a very good approximation at typical belt ply cord angles. At $\alpha = \tan^{-1}\sqrt{2}$, where cord strain is always zero, Equation (15) is exact.

2.3.2 Bending Stiffness

The bending stiffness, EI, is based on rectangular beam theory with average stiffness governed by EA within the belt plies and rubber elasticity within the tread. Consider the composite of N belt plies plus a tread layer sketched in Figure 6. The bending stiffness of the belt plies alone is given by

$$(EI)_b = \frac{EA}{t_b w_b} w_b \frac{(N t_b)^3}{12} \tag{16}$$

The bending stiffness of the tread alone is given by

$$(EI)_t = E_R w_t \frac{t_t^3}{3} \tag{17}$$

Equation (17) places the neutral surface of bending at the base of the tread; this is expected because of the high extensional stiffness of the belt as compared to the tread rubber. The values of w_t and t_t depend on the tread pattern as well as the overall
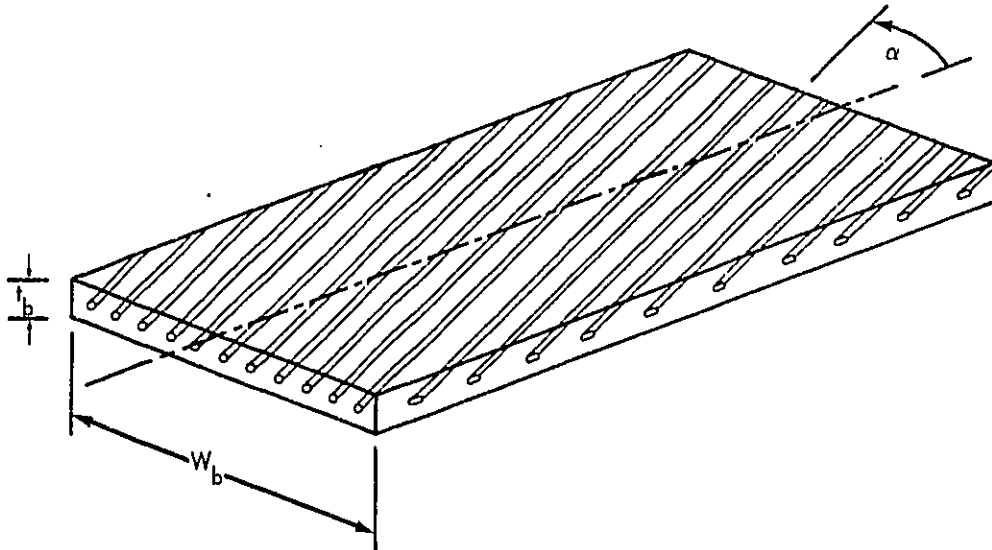
Figure 5. Sketch of Single Belt Ply.
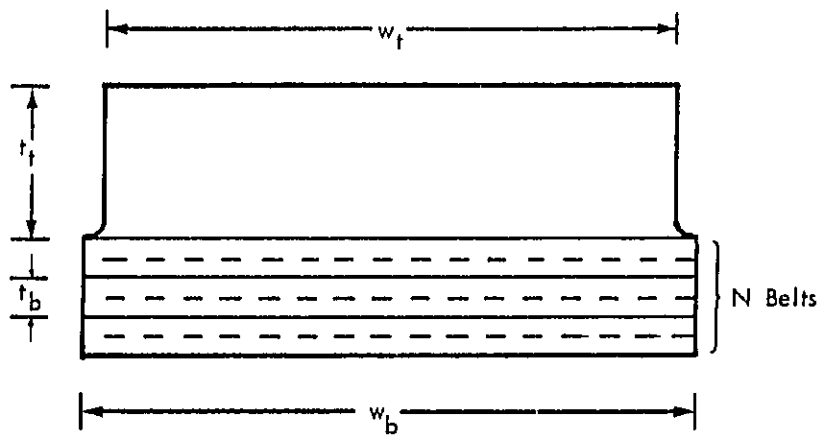
Figure 6. Sketch of Belt Plies and Tread Rubber.

dimensions. If there are circumferential grooves, w_t should represent the effective tread cross-sectional area. If there are lateral grooves, t_t should be measured from the base of the tread rubber to the bottom of the grooves.

2.3.3 Bedding Stiffness

The radial and circumferential bedding stiffness, k_r and k_t, represent the support of the tread area by the sidewalls. The sidewalls support the tire through the effect of inflation pressure. For the purpose of estimating these stiffnesses, the sidewalls may be treated as membranes with circular shape. Referring to the sketch in Figure 7, Bohm derived the following expressions for k_r and k_t:

$$k_r = \frac{\cos \Theta_0 + \Theta_0 \sin \Theta_0}{\sin \Theta_0 - \Theta_0 \cos \Theta_0} \, p_0 \tag{18}$$

$$k_t = \frac{G_R t_s}{l_s} + p_0 \cot \Theta_0 \tag{19}$$

where p_0 is the inflation pressure.

These expressions were derived by considering virtual displacements in the radial and circumferential directions, keeping l_s invariant, and assuming the sidewalls remain arcs of circles. The shear term in Equation (19) is based on the rubber alone, since the shear is transverse to the radial carcass ply direction.

2.3.4 Damping Coefficients

A direct calculation of damping coefficients from detailed construction would be extremely difficult, and would require a model substantially more complex than considered thus far. It is simpler to use experimental measurements of loss to estimate damping, treated here as viscous damping.

Consider a one-dimensional damped oscillator whose equation of motion is

$$m \ddot{x} + d \dot{x} + kx = F(t) \tag{20}$$

The Q factor (inverse of the loss factor, the attenuation per cycle) of this system is given by

$$Q = \sqrt{km} \, / \, d \tag{21}$$

Measurements of reverberant decay times[7] and in-use decay rates[10] indicate that Q is of order 10 for heavy truck tires. Applying Equation (21), noting that the quantities of interest here are per unit length,
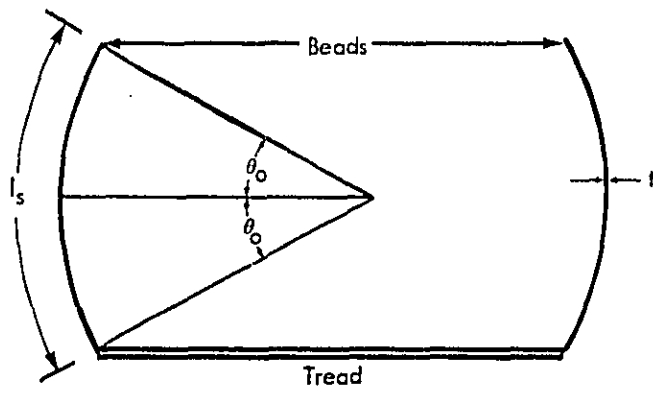
Figure 7. Sidewalls as Circular Membrane Segments.

$$d_r = \sqrt{k_r \mu} / 10 \qquad\qquad (22a)$$

$$d_t = \sqrt{k_t \mu} / 10 \qquad\qquad (22b)$$

where k_r and k_t are given by Equations (18) and (19).

2.4 Calculated Shape of Two Tires

Tables 2 and 3 list pertinent material and dimensional data for two 11R22.5 heavy-duty truck tires.[18] Tire A corresponds to the B.F. Goodrich Milesaver steel-belted radial tires which were tested and reported on in Reference 7. Tire B corresponds to an experimental variation being manufactured for use in a later task of the current project, with the belt stiffened by the reduction of cord angle and addition of an extra belt ply. Table 4 lists the calculated structural properties required for Bohm's equations. Two bending stiffnesses are shown for each tire: with and without the stiffening effect of the tread rubber, corresponding to tread grooves which are predominately circumferential and transverse, respectively.

The shapes and contact patch forces for these two tires were computed using the method described in Section 2.3. Figures 8 and 9 show the calculated curvatures for the transverse groove version of each of these tires running at 35 mph on a smooth flat surface. The calculations used a 200 point mesh in the contact patch for numerical evaluation of the pressure integrals, and include harmonic terms up to $n = 500$. Figures 10 and 11 show the calculated radial contact patch pressure distribution for each tire.

2-18

Table 2

Summary of Material Properties,
B.F. Goodrich Heavy-Duty Radial Truck Tires

Elastic Moduli (psi)		Static	Dynamic
Cord Plies	E_R =	1600	2800
	G_R =	530	940
Tread Rubber	E_R =	950	1640
	G_R =	320	535

Ply Thickness: 3/32 inch

Tread Depth: 19/32 inch

Belt Cords: 0.0472-inch diameter steel, 14 per inch

$$E_S = 3 \times 10^7 \text{ psi}$$

Table 3

Summary of Belt Constructions

Ply No.	TIRE A (Standard)		TIRE B (Modified)	
	Angle	Width	Angle	Width
1	65°R	6 inches	65°R	6 inches
2	21°R	7 inches	18°R	7 inches
3	21°L	6.3 inches	18°L	6.3 inches
4	---	---	18°L	5.5 inches

Table 4

Tire Parameters For Thin-Shell Equations

Quantity (Units)	TIRE A		TIRE B	
	Without Tread*	With Tread	Without Tread	With Tread
EA (lb)	1.19×10^5	1.32×10^5	3.41×10^5	3.54×10^5
EI (lb-ft^2)	5.1	9.3	13.2	17.4
k_r (lb/ft/ft)	1.14×10^5			
k_t (lb/ft/ft)	2×10^4			
d_r (lb/ft/sec^2)	13.4			
d_t (lb/ft/sec^2)	5.6			
T_o (lb)	1.5×10^4			
μ (slug/ft)	0.158			

* Tread is always present. This indicates whether the tread is included when calculating EA and EI.
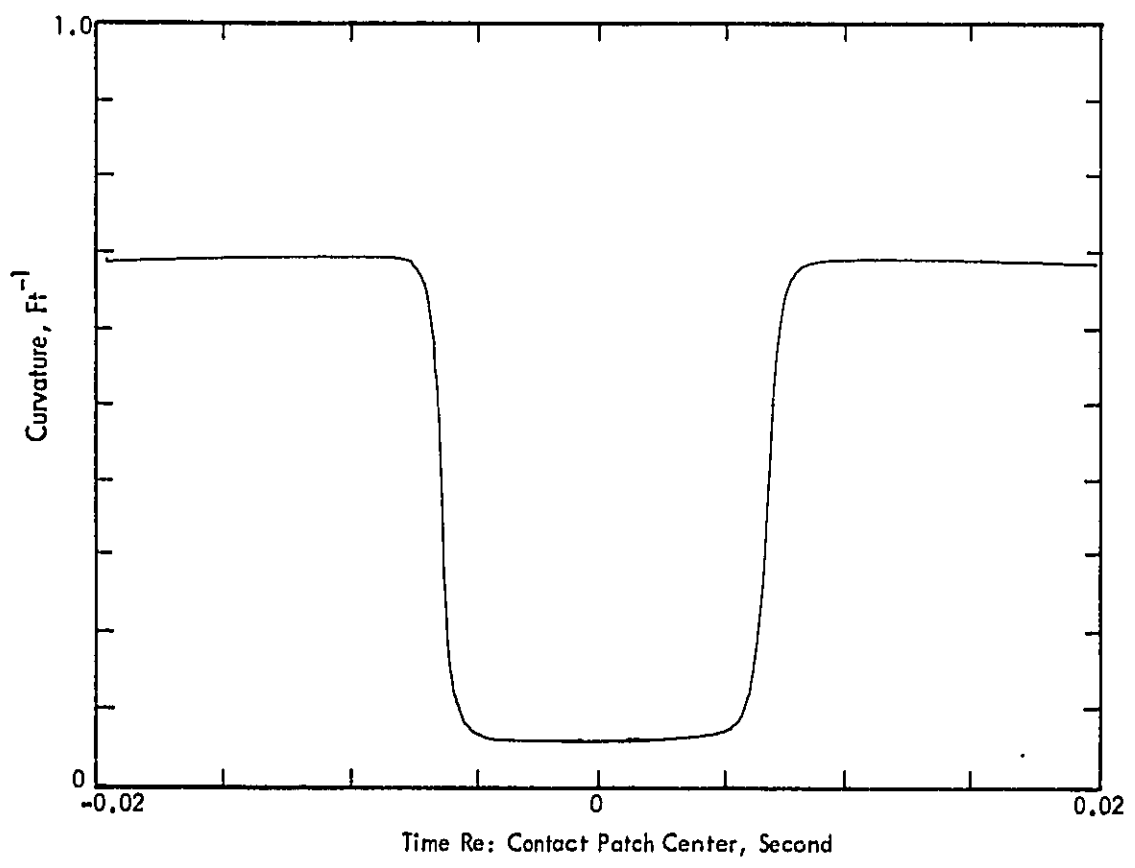
Figure 8. Calculated Tire Curvature. Tire A, Standard Construction.
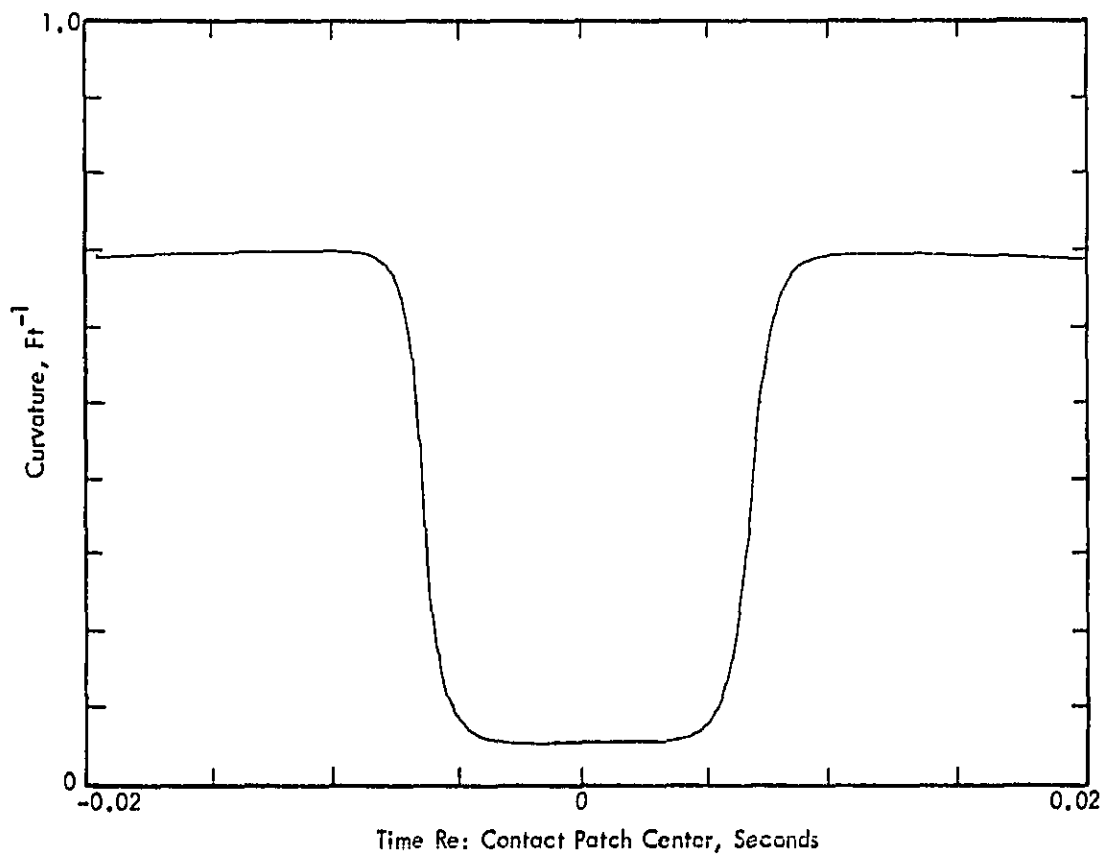
Figure 9. Calculated Tire Curvature. Tire B, Modified Construction.
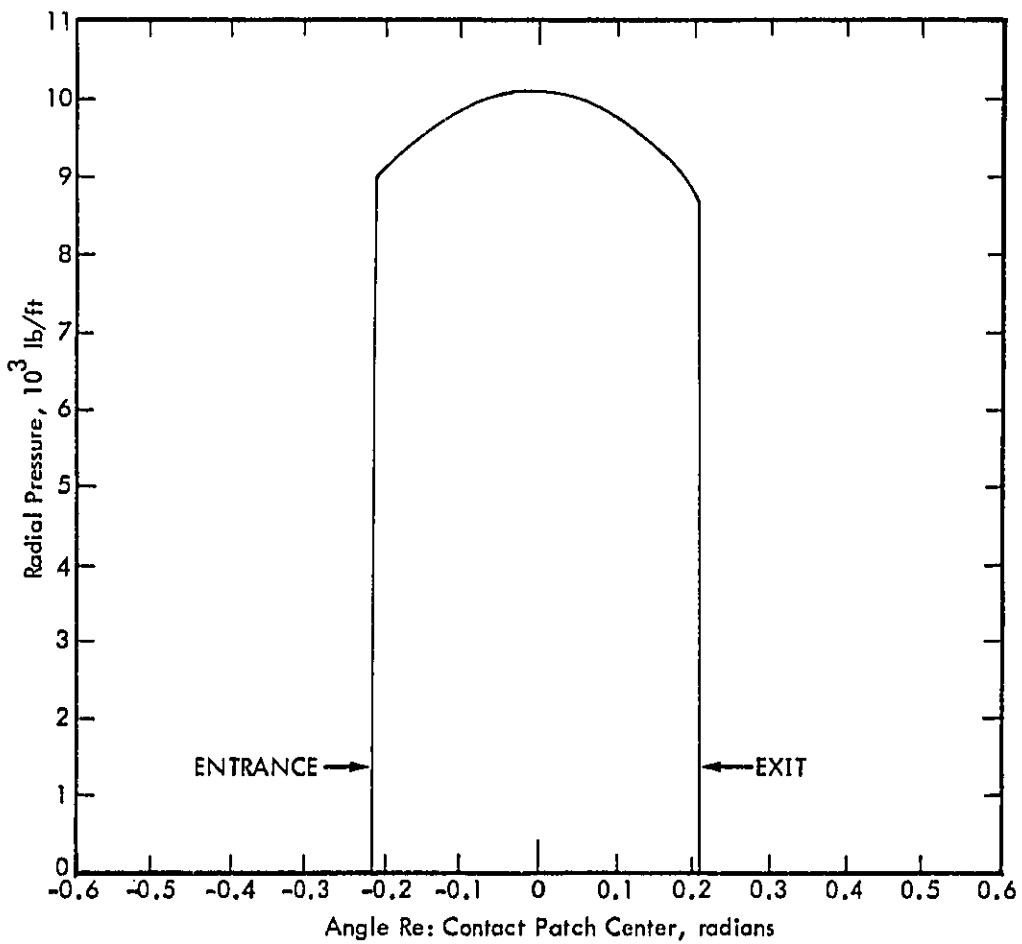
Figure 10. Radial Contact Patch Pressure, Tire A.
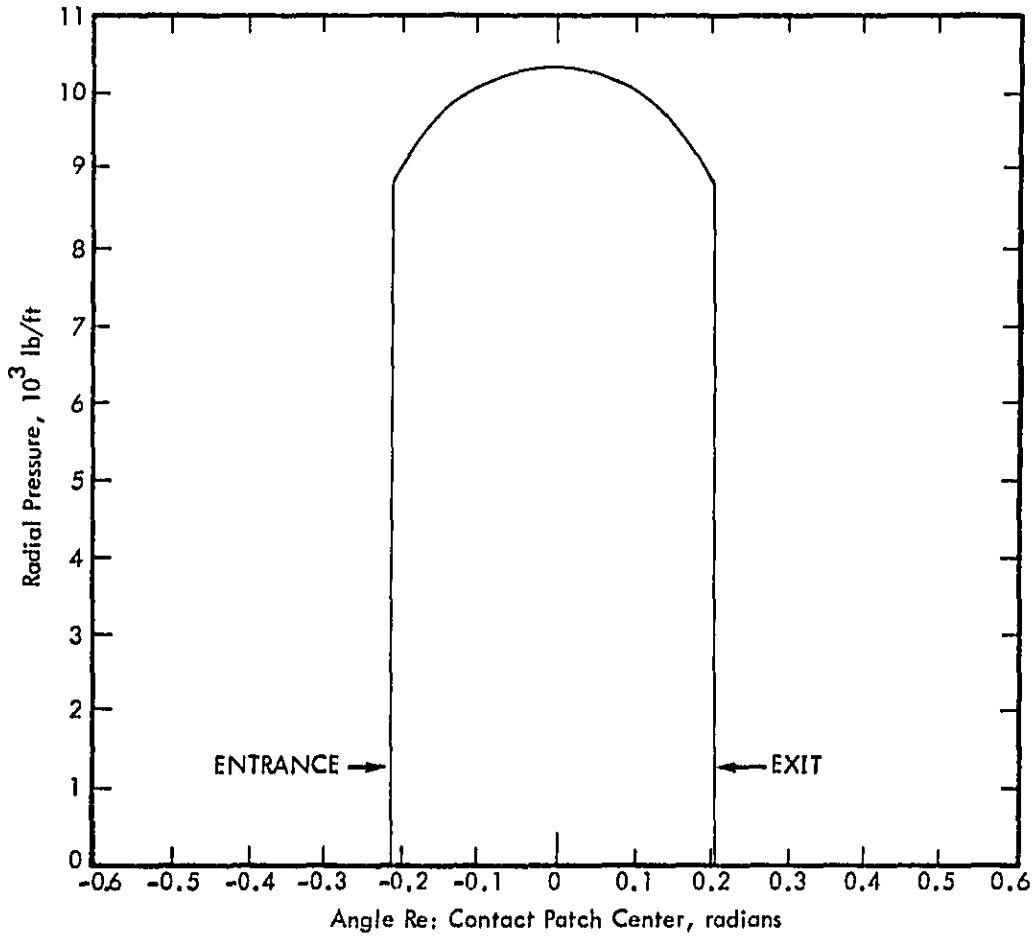
Figure 11. Radial Contact Patch Pressure, Tire B.

3.0 AIR PUMPING

The phenomenon of air pumping, first identified by Hayden,[19] is based on the existence of monopole sound sources associated with unsteady air flow from tread voids. The sound pressure radiated from a monopole into free space is

$$p = \frac{\rho \ddot{V}}{4\pi r} \tag{23}$$

where r is the source-receiver distance. When applied to tires, the key parameter required is the second derivative of volume pumped, $\ddot{V}$. Early attempts to estimate $\ddot{V}$ based on vertical compression of the tread rubber did not yield satisfactory results. Recent experimental results by Plotkin, et al.,[7] and Samuels,[20] which involved direct measurement of $\ddot{V}$, showed excellent agreement with Equation (23). A significant finding in both of these studies is that tread void compression occurs primarily through lateral motion of tread elements entering and leaving the contact patch; vertical compression of the tread rubber is a secondary or negligible effect. Void volume may be computed by assuming tread blocks to maintain their original shape, but with their spacing varying as the shape of the tire changes through the contact patch. An additional consequence of this direct relation to the shape of the carcass is that $\ddot{V}$ may be replaced by $V'' U^2$. This leads directly to the $40 \log_{10} U$ speed dependence first predicted by Hayden and very often seen experimentally.

Two other phenomena must be considered. First, a tire does not operate in free space: there are reflections from the ground and from the tire itself. In the near field to the side of the tire, the reflection from the ground and the tire sidewall raises the pressure by a factor of approximately 4; this factor depends on the ratio between wavelength and tire dimension. In general, Equation (23) must be multiplied by a geometric radiation factor G. Second, when considering a rib tire with continuous grooves, some of the displaced air moves within the grooves, and does not pump out of the tire. The amount which does lead to sound radiation is proportional to the fraction of flow blockage, ϵ. It was shown in Reference 7 that for typical rib tires $\epsilon \approx 0.35$. For a crossbar-type void, open only at one end, $\epsilon = 1$.

The following subsections present the basic derivation of air pumping for simple lateral tread grooves, and the generalization to full tread patterns.

3.1   Air Pumping From Lateral Grooves

Consider a tread pattern consisting of lateral grooves and tread blocks as shown in Figure 12. Assuming that the block volumes do not change, and that the centerline of
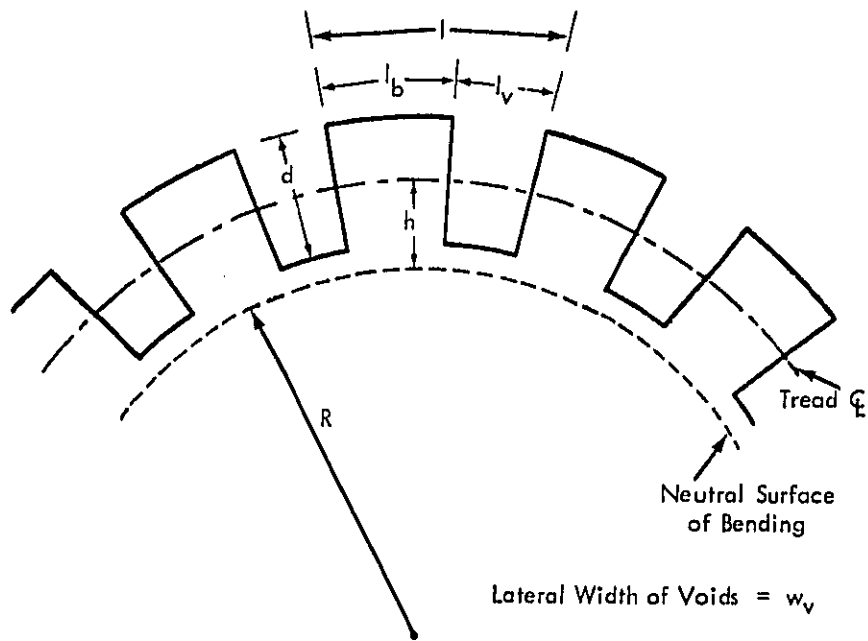
Figure 12. Geometry of Lateral Tread Voids.

each block remains normal to the neutral surface of bending as R changes, the volume of a single void is given by

$$V = w_v d \left[l_v - l_b h \kappa_0 + (l_v + l_b) h \kappa \right] \tag{24}$$

where $\kappa = 1/R$ = curvature, and κ_0 corresponds to the undisturbed curvature $1/R_0$. The derivation of Equation (24) carries the implicit assumption that the pitch length l (distance between repetitions of similar tread elements) is small compared to changes in curvature. Note also that the functional dependence of V on κ depends on total pitch length, not just block or void size alone. Even though Equation (24) describes the volume of a single void, it is a single void in a full tread pattern. A single void cut in a blank tire would have quite different behavior, with detailed deformation of the surrounding rubber playing an important role.

The quantity required is $\ddot{V}$. Noting that all parameters in Equation (24) except κ are constant, and that κ is a function of φ,

$$\ddot{V} = V'' (\varphi) \, \Omega^2 = w_v \, d \, (l_v + l_b) h \, \frac{d^2 \kappa}{d \varphi^2} \, \Omega^2 \tag{25}$$

The shape of the tire is given by $R_0 + w(\varphi)$, with $w(\varphi)$ given by the solution to the stationary shape equations. The curvature of a curve in r, φ coordinates is given by

$$\kappa = \frac{r^2 + 2 (r')^2 - r r''}{\left[r^2 + (r')^2 \right]^{3/2}} \tag{26}$$

Taking the second derivative of κ with respect to φ, substituting $R_0 + w$ for r, and retaining terms to first order in w,

$$\kappa'' = - \frac{w'' + w^{iv}}{R_0^2} \tag{27}$$

The derivatives of w are straightforward to obtain from Equation (3). The final expression for sound pressure p as a function of φ, the instantaneous position of the void, is (using Equation 23)

$$p(\varphi) = - \frac{G \epsilon \rho}{4 \pi r} \left(\frac{U}{R_0} \right)^2 w_v \, d \, h \, (l_v + l_b) \, \frac{1}{R_0^2} \tag{28}$$

$$\bullet \sum_{n=1}^{\infty} n^2 (n^2 - 1) (C_n \sin n\varphi + D_n \cos n\varphi)$$

3-3

where Ω has been replaced by U/R_o. The sound pressure as a function of time is given by $p(\varphi_o + \Omega t)$, where φ_o is the position of the void at $t = 0$.

A computer program has been prepared which reads C_n and D_n from a file written by the shape calculation program. These are invariant for a given carcass design, speed, and load. The tread parameters are read from a separate input data file. Sound pressure and corresponding sound pressure level are calculated over a range of time specified by the user. The program includes two details not explicitly noted above:

- The source-receiver distance r is a function of φ. Large values of κ'' exist over a small region, so there is generally little effect on signature shape as r varies with φ. By including an exact calculation for r in the program, however, the correct distance to the major part of the source is automatically accounted for.

- The sound pressure received at a given time is actually $p(\varphi_o + \Omega t + \Omega r/a)$, since it takes time r/a for sound to propagate from the source to receiver. The program has the capability of making this phase correction. The calculation becomes more complex, however, since time can no longer be treated as an independent variable. This adjustment is therefore treated as an option used only when necessary.

Figure 13 shows calculated air pumping per void for a 0.75-inch-deep by 3-inch-wide grooves with 2.75-inch pitch cut into tires A and B. The geometric radiation factor G is not included, but will be essentially the same for each tire.

3.2   Air Pumping From a Full Tread Pattern

Once air pumping is computed from Equation (28) for a given tire and cross-groove pattern, it is straightforward to scale it to other tread dimensions for the same tire carcass. If the air pumping sound pressure is $p_o(t)$ for a tread void with pitch l_o ($l = l_v + l_b$), depth d_o and width w_o, then the sound pressure for a tread void with dimensions l_1, d_1, and w_1 is

$$p_1(t) = \frac{l_1 \, d_1 \, w_1}{l_o \, d_o \, w_o} \, p_o(t) \qquad (29)$$

Equation (29) applies equally to the expression for sound pressure p(t) which includes the phase adjustment $\Omega r/a$.
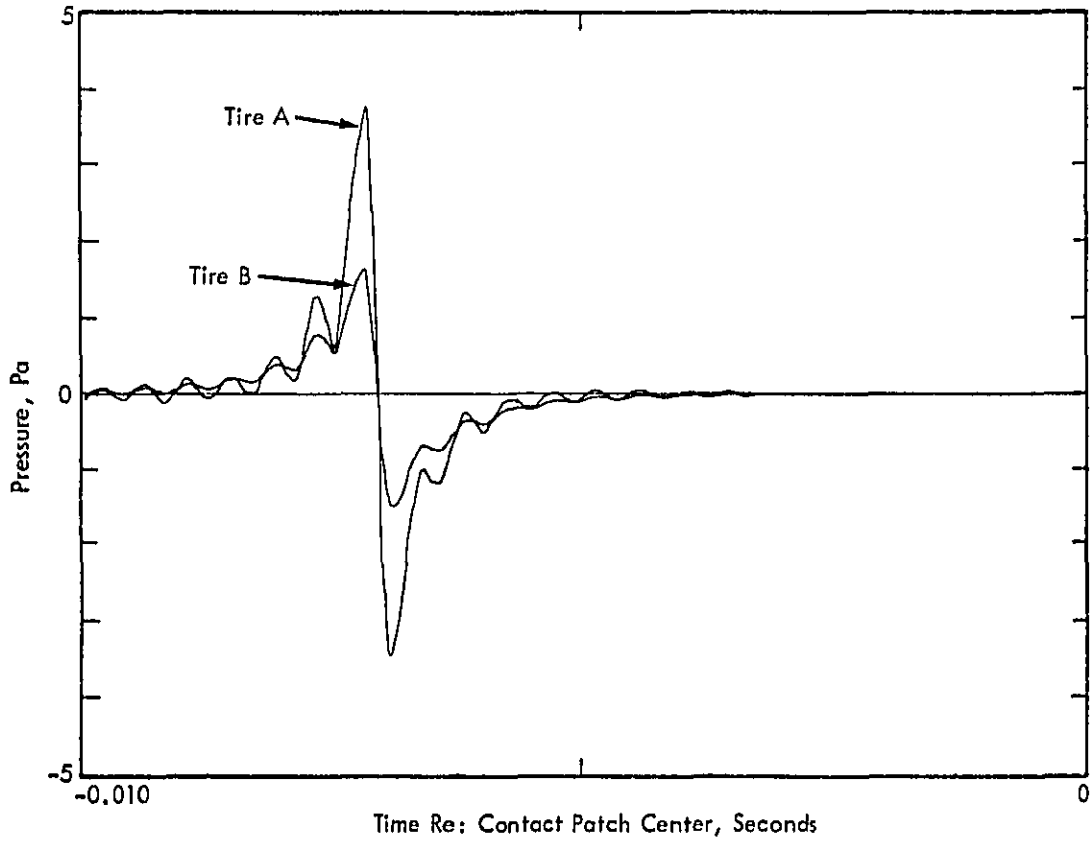
Figure 13. Predicted Air Pumping Per Void, Lateral Groove.

If void 1 is located at ϕ_1 and void 0 at ϕ_0, the time coordinate is adjusted by $(\phi_1 - \phi_0)/\Omega$. If there is a series of grooves spaced at intervals $\Delta\phi$, then Equation (29) is summed over all grooves with a time shift of $\Delta\phi/\Omega$ between signatures.

The assumptions of ring behavior of the belt and negligible compressibility of the tread rubber lead to the conclusion that Equations (28) and (29) apply equally well to a small lateral section of a groove which runs across the tire at an angle other than 90°. The air pumping from an oblique groove may therefore be obtained by writing Equation (29) for each differential width element and integrating across the tire. Consider a tread pattern consisting of a uniform cross-section groove whose shape is defined by $y_g(x)$, where $x = 0$ at the centerline of the tire and y_g has sense opposite to ϕ. (Referring to the coordinates in Figure 1, the tire would leave a footprint whose shape corresponds to $y_g(x)$ in the x,y ground plane.) Returning to the use of ϕ as the independent variable, the sound pressure from such a groove is

$$ p(\phi) = \frac{1}{w_t} \int_{-w_t/2}^{w_t/2} p_o(\phi - y_g(x)/R_o) \, dx \qquad (30) $$

where p_o is the pressure for a full-width 90° void of similar pitch and depth located at $\phi = 0$ when $t = 0$. If there is a full tread pattern defined by N voids of shape $y_{gi}(x)$, then the total air pumping noise is

$$ p(\phi) = \frac{1}{w_t} \sum_{i=1}^{N} \int_{-w_t/2}^{w_t/2} p_o(\phi - y_{gi}(x)/R_o) \, dx \qquad (31) $$

Equation (31) may be treated as a function of time by the relation $\phi = \Omega t$.

The air pumping computer program includes Equation (31). Any number of tread voids may be defined, with $y_{gi}(x)$ specified as a set of points. The calculation is applicable to rib tires as well as cross-groove. When defining elements for a rib tire, they should in general correspond to the straight segments between corners. The flow blockage ϵ must also be specified so as to account for the fact that flow blockage successively increases as each element goes further into the contact patch.

4.0 CARCASS VIBRATION AND RADIATION

The tire models discussed thus far consider only the steady behavior of a uniform carcass on a smooth surface. A treaded tire on a textured surface experiences unsteady loads in the contact patch. These lead to vibrations which radiate sound. The radiation of sound by carcass vibration appears to be the major source of noise to the rear of heavy truck tires. The most important radiating area has been identified to be the tread area within one foot of the contact patch exit.[7,10] Treating this area as a piston,[7] and as a simple damped travelling wave,[10] and using experimentally measured vibration levels has given very good agreement with measured near-field tire noise levels. A key step of the set of models developed in this study is obtaining vibration levels directly from the tire, tread, and road surface properties. The following subsections describe models for the vibrating motion of a tire in the region important for sound radiation, the excitation of this vibration by the tread/road interface, and the radiation of sound due to this motion.

4.1 Vibratory Motion of Tire Carcass

The thin shell relations, Equations (1), describe the full time-dependent motion of a tire. Solution of these equations can be quite difficult; consider, for example, the complexity of the the steady-state solution presented in Section 2.2. There are two physical parameters which permit substantial simplification of the equations:

- Frequencies of interest are in the audio range, generally above 100 Hz. The rotational speed of a truck tire at 35 to 55 mph is 5 to 8 Hz. The equation may therefore be considered in the limit $\partial/\partial t \gg \Omega$.

- An area of about one-tenth the circumference of the tire is important. Over this distance, the curvature of the belt can be neglected.

Considering the limit $\partial/\partial t \gg \Omega$, all terms in Equations (1) with a factor Ω may be eliminated. This removes all centripital and Coriolis terms. While important for the stationary shape calculation, they are negligible at audio frequencies. If the circumferential coordinate is also changed from ϕ to $s = R_o \phi$, then Equations (1) become

$$\mu \ddot{V} - EA \left(V'' + \frac{1}{R_o} w' \right) + k_t V - d_t V' = 0 \tag{32a}$$

$$\mu \ddot{w} + \frac{EA}{R_o^2} (R_o V' + w) + EI \left(w^{iv} + \frac{2}{R_o^2} w'' + \frac{w}{R_o^4} \right)$$

$$- T_o \left(w'' + \frac{w}{R_o^2} \right) + k_r w + d_r \dot{w} = 0 \tag{32b}$$

4-1

where ( )' now denotes $\partial/\partial s$. The external pressures p_r and p_t have been set equal to zero because the area of interest is outside the contact patch. The vibratory excitation will be handled by a boundary condition at the contact patch edge.

Since the important vibratory motion occurs over a short range of s, it follows that $\partial/\partial s \gg 1/R_0$. Neglecting terms of order $1/R_0$, Equations (32) become

$$\mu \ddot{v} - EA\, v'' + k_t\, v - d_t\, \dot{v} = 0 \tag{33a}$$

$$\mu \ddot{w} + EI\, w^{iv} - T_0\, w'' + k_r\, w + d_r\, w = 0 \tag{33b}$$

The w and v motions are independent in this limit. Equation (33b) is identical to the form Eberhardt[10] postulated for interpretation of phase velocity, with the addition of the damping term.

For the case of excitation at the contact patch edge, the solution to Equation (33b) at frequency ω may be written

$$w = W\, e^{i(k_t s - \omega t)}\, e^{-\eta s} \tag{34}$$

where s is measured away from the contact patch edge, and W is determined from the forced motion of the edge of the contact patch. The wave number k_t and decay factor η are determined from:

$$k_t = \omega/C_p \tag{35}$$

$$C_p^2 = \frac{1}{\mu}\left(EI\, k^2 + T_0 + \frac{K_r}{k_t^2}\right) \tag{36}$$

$$\eta = \frac{C_p\, k_r}{(4\, EI\, k_t^2 + 2\, t_0)} \tag{37}$$

The physical parameters used in Equations (34) through (37) are identical to those used in Section 2 for calculation of the stationary shape. One difference in application is that η in Equation (34) is directly related to the loss factor: $\eta = k_t/4\, Q$. The empirical value of $Q = 10$ may be used rather than the deduced value of k_r. The high-frequency behavior of the belt area includes losses which are not treated by consideration of k_r alone.

Figure 14 shows calculated phase velocities for the tires described in Table 2. Also shown are measured phase velocities for two examples of production versions of tire
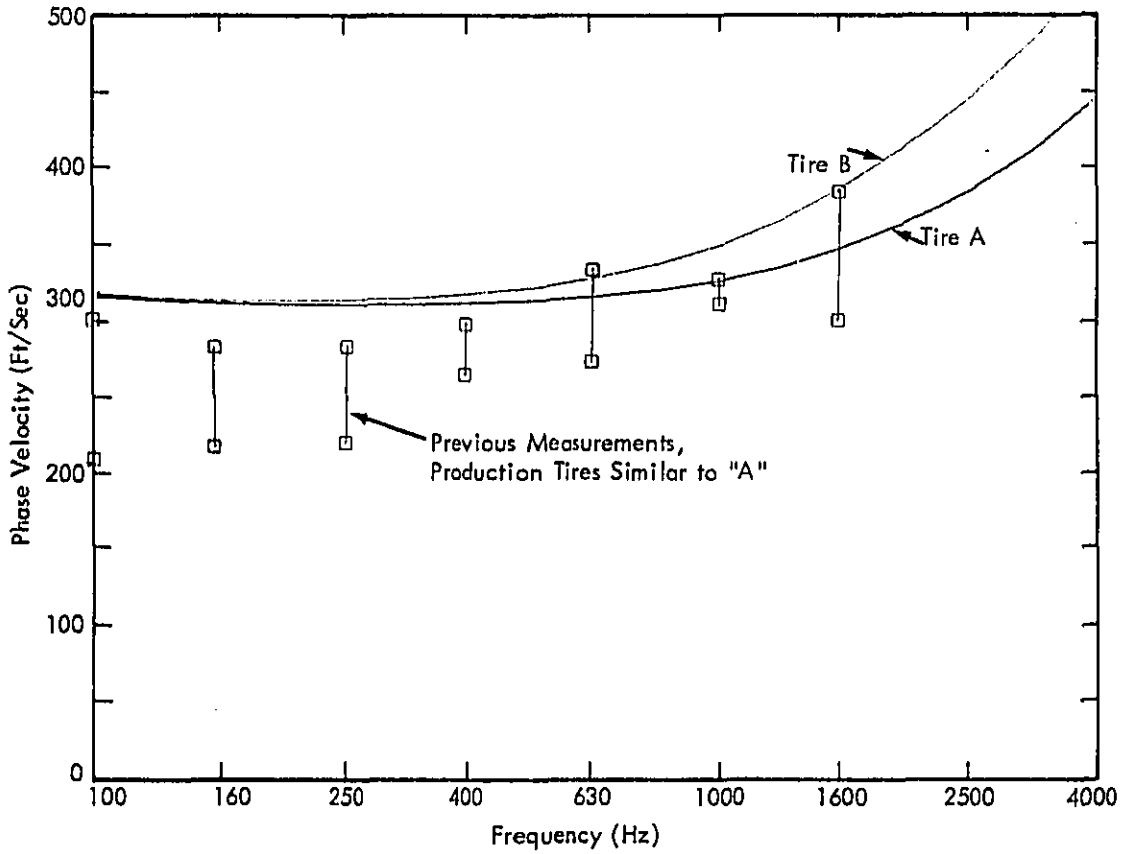
Figure 14. Calculated Phase Velocities For Experimental Tires.

construction A. The measured phase velocities were obtained from transfer functions calculated from the static vibration test data reported in Reference 7. The phase velocity agreement is quite good, lending confidence to the validity of this model.

A detail which was removed from the equations of motion when obtaining Equations (33) is the fact that the tire is moving. In a frame of reference moving with the tread belt, this may be restored by arranging the boundary conditions – which define amplitude W – to move at the tire speed in the -s direction. In a fixed frame, this is equivalent to adding the tire velocity to the phase velocity. The computerized implementation of Equations (34) through (37) includes this convection adjustment. The tire speed is added to C_p following the contact patch and subtracted ahead of it.

4.2 Vibrational Excitation

4.2.1 Excitation Due to Tread Pattern

Consider a tread pattern whose circumferential distribution of tread area may be written $A(\phi_o)$, where ϕ_o corresponds to ϕ at $t = 0$. The differential area over a circumferential increment $d\phi_o$ is given by $A(\phi_o)d\phi_o$. The differential force increment at a position ϕ is given by

$$dF(\phi) = p(\phi) A(\phi - \Omega t) d\phi \tag{38}$$

where $p(\phi)$ is the radial force in the contact patch as calculated in Section 2.0. Equation (38) is written as a ring model, with uniform transverse properties. It is straightforward to consider this relation to be generalized such that $p(\phi)$ is the pressure averaged laterally across the tire, and A is a lateral average of the geometric tread area times a weighting function representing the actual lateral pressure distribution. A typical lateral pressure distribution is shown in Figure 2.

The quantity which is directly related to sound radiation is the radial acceleration of the tire. The motion of the tire at a point ϕ_1 is given by $f(\phi - \phi_1)$ times the force at ϕ, where f is as defined in Section 2. Thus,

$$dw(\phi_1) = f(\phi - \phi_1) p(\phi) A(\phi - \Omega t) d\phi \tag{39}$$

Integrating Equation (39), the motion at ϕ_1 is

$$w(\phi_1) = \int_0^{2\pi} f(\phi - \phi_1) p(\phi) A(\phi - \Omega t) d\phi \tag{40}$$

The acceleration at ϕ_1 is given by

$$\ddot{w}(\phi_1) = \Omega^2 \int_0^{2\pi} f(\phi - \phi_1)\, p(\phi)\, A''(\phi - \Omega t)\, d\phi \qquad (41)$$

It must be kept in mind that Equation (41) is a dynamic result based on the static behavior of the tire; it assumes that the effect of loads at ϕ are instantly transmitted to ϕ_1. Since ϕ_1 of interest is at the edge of the contact patch, and ϕ of interest is within the contact patch, the distances are generally small. The assumption becomes more reasonable as $\phi \to \phi_1$, so that Equation (41) will be most accurate when predicting motion at one contact patch edge due to excitation at that edge. Physically, this should be the most important component. The final result for excitation will be examined to check this condition.

Integrating Equation (41) by parts, and noting the cyclic nature of the integral,

$$\ddot{w}(\phi_1) = -\Omega^2 \int_0^{2\pi} f'(\phi - \phi_1)\, p(\phi)\, A'(\phi - \Omega t)\, d\phi$$

$$\qquad (42)$$

$$-\Omega^2 \int_0^{2\pi} f(\phi - \phi_1)\, p'(\phi)\, A'(\phi - \Omega t)\, d\phi$$

Integrating the first integral by parts, the following is obtained:

$$\ddot{w}(\phi_1) = \Omega^2 (I_1 + I_2) \qquad (43)$$

where

$$I_1 = \int_0^{2\pi} f''(\phi - \phi_1)\, p(\phi)\, A(\phi - \Omega t)\, d\phi$$

$$I_2 = \int_0^{2\pi} \left[f'(\phi - \phi_1)\, A(\phi - \Omega t) - f(\phi - \phi_1)\, A'(\phi - \Omega t) \right] p'(\phi)\, d\phi$$

Equations (42) and (43) are forms which may be numerically integrated: f and p are known from the stationary shape calculation, and A is known from the tread geometry. The integration by parts eliminates the second derivative of A, which can be numerically troublesome. Rather than adopt a "brute force" approach of numerical integration, however, it is worth simplifying these expressions based on known properties of f and p.

Figures 15 and 16 show f' and f'', respectively, corresponding to f in Figure 3. There is a strong peak in f'' about $\phi = \phi_l$. Integral I_l will have its maximum contribution at this point. Thus

$$I_l \approx \Delta f'(0)\ p(\phi_l)\ A(\phi_l - \Omega t)$$

where $\Delta f'(0) = f'(0+) - f'(0-)$. The point at which ϕ_l is of interest is just outside the contact patch, where $p = 0$. Thus, $I_l \approx 0$.

The contact patch pressure rises very sharply at the edges, so that I_2 will be dominated by the integrand near the edges. Approximating $p(\phi)$ by a step function:

$$p(\phi) = P\left[H(\phi - \phi_a) - H(\phi - \phi_b)\right]$$

where ϕ_a and ϕ_b are the contact patch entrance and exit, respectively, $\ddot{w}$ becomes

$$\ddot{w}(\phi_l) = P\Omega^2 \left[f'(\phi_a - \phi_l)\ A(\phi_a - \Omega t) - f(\phi_a - \phi_l)\ A'(\phi_a - \Omega t) \right.$$
$$\left. - f'(\phi_b - \phi_l)\ A(\phi_b - \Omega t) + f(\phi_b - \phi_l)\ A'(\phi_b - \Omega t) \right] \tag{44}$$

Consider the motion at one edge of the contact patch; ϕ_b, for example. The term $f'(\phi_b - \phi_l)$ becomes $f'(0) \approx 0$. Referring to Figures 3 and 15, the terms $f(\phi_a - \phi_b)\ A'$ and $f'(\phi_a - \phi_b)\ A$ are small compared to $f(0)\ A'$ for any tread with a reasonably aggressive tread and pitch smaller than the contact patch length. Equation (44) is thus dominated by the $f(0)\ A'$ term. Thus the motions at the contact patch edges are

$$\ddot{w}(\phi_a) = P\Omega^2\ f(0)\ A'(\phi_a - \Omega t)$$

$$\ddot{w}(\phi_b) = P\Omega^2\ f(0)\ A'(\phi_b - \Omega t) \tag{45}$$

The motion at a contact patch edge is thus dominated by tread impacts at that edge. This is the condition for which the use of the steady quantity $f(\phi - \phi_l)$ is most valid. As a qualitative additional support for this simplification of Equations (44) into (45), the use of $f(\phi - \phi_l)$ would tend to overstate the motion at a point away from the excitation, so that the neglected terms $f'(\phi_a - \phi_b)\ A$ and $f(\phi_a - \phi_b)\ A'$ here are probably larger than the correct ones in a more exact derivation.

Equations (45) are physically equivalent to the tread impulse models in use in the tire industry as the basis of tread randomization programs. They go one step further in that the amplitude of the vibration input, as well as its spectral properties, is obtained. These equations form the basic vibration input element of the noise models. The

4-6
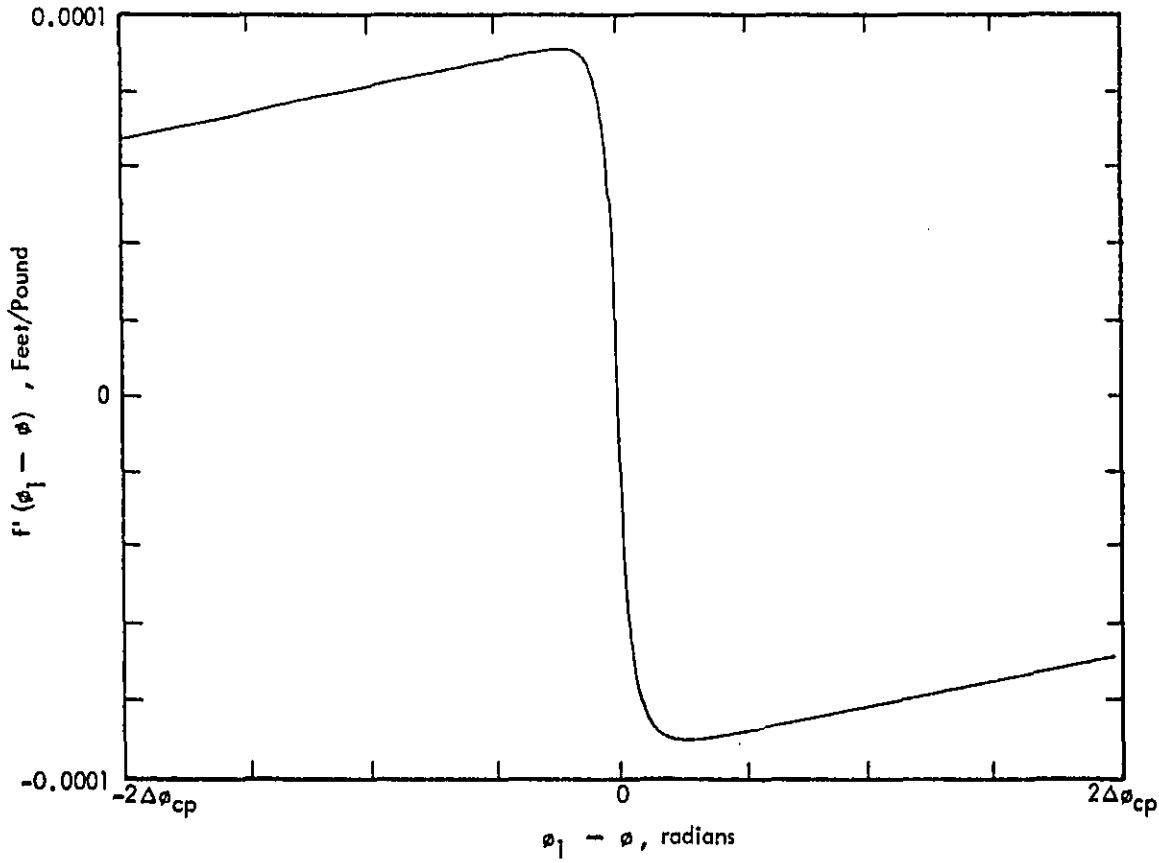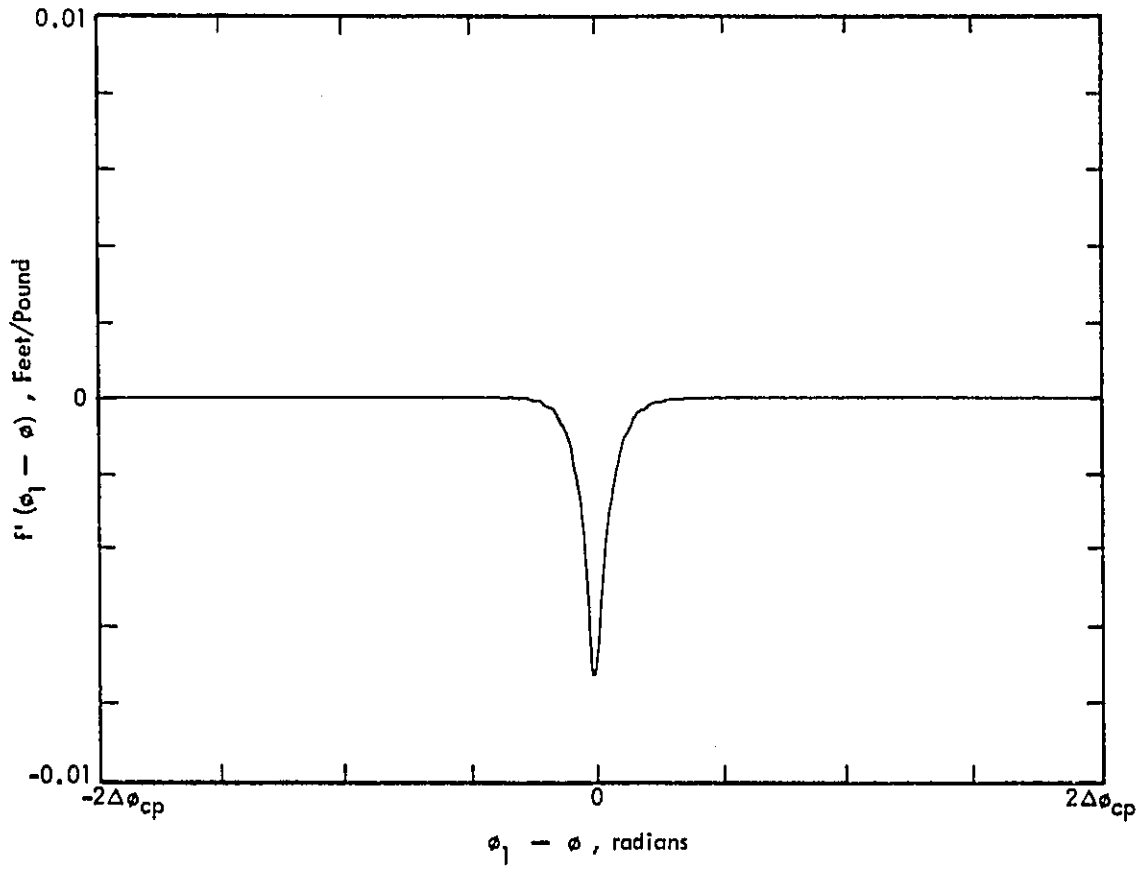
Figure 15. $f'(\phi_1 - \phi)$, Tire A.

Figure 16. f"$(\phi_1 - \phi)$, Tire A.

amplitude W required for the vibration response, Equation (34), is directly obtained from the Fourier transform of A'.

In the computational system, f (0) is obtained from the programs which compute the stationary shape of the tire, as discussed in Section 2.2. A' is computed from the tread geometry. It is a specialized calculation for each tire, and is treated as an input quantity. The spectral values of A' at particular frequencies are obtained by numerically computing the Fourier coefficients of A'.

4.2.2 Excitation Due to Pavement Texture

Consider a pavement with a surface texture described by $z_s(x,y)$, the height of a point above the mean. If a tire tread compresses linearly to conform to the pavement, as suggested by Nilsson,[9] and the average total compression under load P is Δz, then the load at a point x,y is given by

$$P_r(x,y) = P\left(1 + \frac{z_s(x,y)}{\Delta z}\right) \tag{46}$$

As pointed out in Reference 21, direct conformation between rubber and pavement, and a linear relationship, is not entirely realistic. The effect of pavement roughness at a point is spread out, in a microscopic equivalent to the function f. If $z_s(x,y)$ is combined with this extended reaction at each point, Equation (46) may be written

$$P_r(x,y) = P\left(1 + \zeta(x,y)\right) \tag{47}$$

where $\zeta(x,y)$ is the combined function. Calculation of ζ from first principles would be extremely difficult. It is clear, however, that the largest scale features would be similar to those of $z_s/\Delta z$. Considering $z_s/\Delta z$ to be a first estimate, and the actual behavior (through the microscopic f) to be smoothed out, ζ would look much like $z_s/\Delta s$ modified by a low-pass filter. A reasonable first approximation to ζ would therefore be $z_s/\Delta z$, smoothed by a scale length comparable to the scale estimated in Reference 21.

With ζ defined by the surface macrotexture and the extended reaction properties of the tread rubber, Equation (38) for the load on an element of the tire may be extended as

$$dF(\phi) = p(\phi)\, A(\phi - \Omega t)\left[1 + \zeta\big(s_0 + R(\phi - \Omega t)\big)\right]d\phi \tag{48}$$

where s_0 is related to the initial position of the tire at time 0, and $\zeta = \zeta(s)$ is a one-dimensional version of $\zeta(x,y)$. The coordinate s is in the -y direction (see Figure 1); its sense is chosen so as to match the direction of $A(\phi_0)$.

Equation (48) may be carried through an analysis identical to that from Equations (38) through (45), with $A(1 + \zeta)$ replacing A. This gives, for the area following the contact patch,

$$\ddot{w}(\phi_b) = P \Omega^2 f(0) \left\{ A'(\phi_b - \Omega t) \left[1 + \zeta \left(s_0 + R(\phi_b - \Omega t) \right) \right] \right.$$
$$\left. + A(\phi_b - \Omega t) \zeta' \left(s_0 + R(\phi_b - \Omega t) \right) R \right\}$$

(49)

If it is assumed for simplicity that $\zeta \ll 1$ and that $A \approx constant$ when compared with ζ', then

$$\ddot{w}(\phi_b) = P \Omega^2 f(0) \left[A'(\phi_b - \Omega t) + \bar{A} \zeta' \left(s_0 + R(\phi_b - \Omega t) \right) R \right]$$ (50)

The assumptions leading to Equation (50) essentially make the effects of tread and texture independent and directly additive. The effect of texture is seen to have an effect identical to that of tread. This is also clearly the case in Equations (48) and (49).

This result suggests that increased pavement texture on a course scale should increase tire noise and also decrease differences between various tread patterns. This is exactly the result experimentally obtained by Thrasher, et al.,[22] and Walker.[23] In these two studies, various tires ranging from blank to traction-type cross-groove were run on different pavement textures. The pavements had textures which visibly varied in courseness. The noise levels showed a strong tendency to increase and to exhibit lower tire-to-tire variation with increasing roughness. Individual deviations from these trends were generally associated with tread patterns which were not necessarily dominated by vibration, such as crossbar tires which exhibited significant air pumping.

In the noise models, ζ and ζ' are treated as inputs, similar to the handling of A and A'.

4.3 Radiation of Sound From a Vibrating Carcass

The relations presented in Sections 4.1 and 4.2 define the motion of the belt area in the vicinity of the contact patch. The sound pressure radiated from a moving surface S is given by[24]

$$p(\vec{r}) = \int_S G(\vec{r}|\vec{r}') (\vec{\nabla}p \cdot \hat{n})' dS$$ (51)

If motion at a single frequency is being considered, this becomes

$$p(\vec{r}, \omega) = -i\omega\rho \int_S G(\vec{r}|\vec{r'}) \, u_n(\vec{r'}) \, dS \qquad (52)$$

The radial velocity u_n is $\dot{w}$ as computed from Equation (34), with amplitude W determined from the analysis of Section 4.2. The appropriate Green's function depends on the geometry considered. Eberhardt[10] successfully used a Green's function corresponding to a vibrating plate (the flattened tread area) in an infinite baffle. Adopting this approach, and substituting Equation (34), Equation (52) becomes

$$p(\vec{r}, \omega) = \frac{\rho W}{2\pi} \, \omega^2 \, e^{-i\omega t} \int_{-w_b/2}^{w_b/2} \int_0^\infty \frac{e^{ik_a r}}{r} \, e^{ik_t s} \, e^{-\eta s} \, ds \qquad (53)$$

Note that the nomenclature k_t denotes wave number in the tire; k_a denotes wave number in air.

It is convenient to normalize Equation (53) by the acceleration $\ddot{w}$ at the contact patch edge. Equation (53) becomes

$$\frac{p(\vec{r}, \omega)}{\ddot{w}(0)} = -\frac{\rho}{2\pi} \int_{w_b/2}^{w_b/2} \int_0^\infty \frac{e^{ik_a r}}{r} \, e^{ik_t s} \, e^{-\eta s} \, dx \, ds \qquad (54)$$

A computer program has been prepared which calculates Equation (54) as a function of frequency and position, for the tire structural parameters defined earlier. A two-dimensional Romberg[25] integration scheme is used to perform the area integrals.

Figures 17 and 18 show the calculated normalized radiations for the two example tires discussed earlier. Shown on each figure is the radiation one foot ahead of and following the contact patch edge, along the tire centerline and three inches from the tread belt. This corresponds to the microphone position considered in Reference 7 for the discussion of carcass radiation. The calculation of actual sound pressure would require a geometric factor (as discussed in Section 2) as well as a value of $\ddot{w}(0)$. The present discussion is primarily concerned with comparisons of radiated sound; the absolute pressures are of secondary interest at this time. Quantitative validation of this mechanism is documented in References 7 and 10. Note that the radiations are virtually the same for both tires, and that radiation is greater to the rear of the tire than ahead of it. This latter result is fully consistent with experimental findings.[7,10]
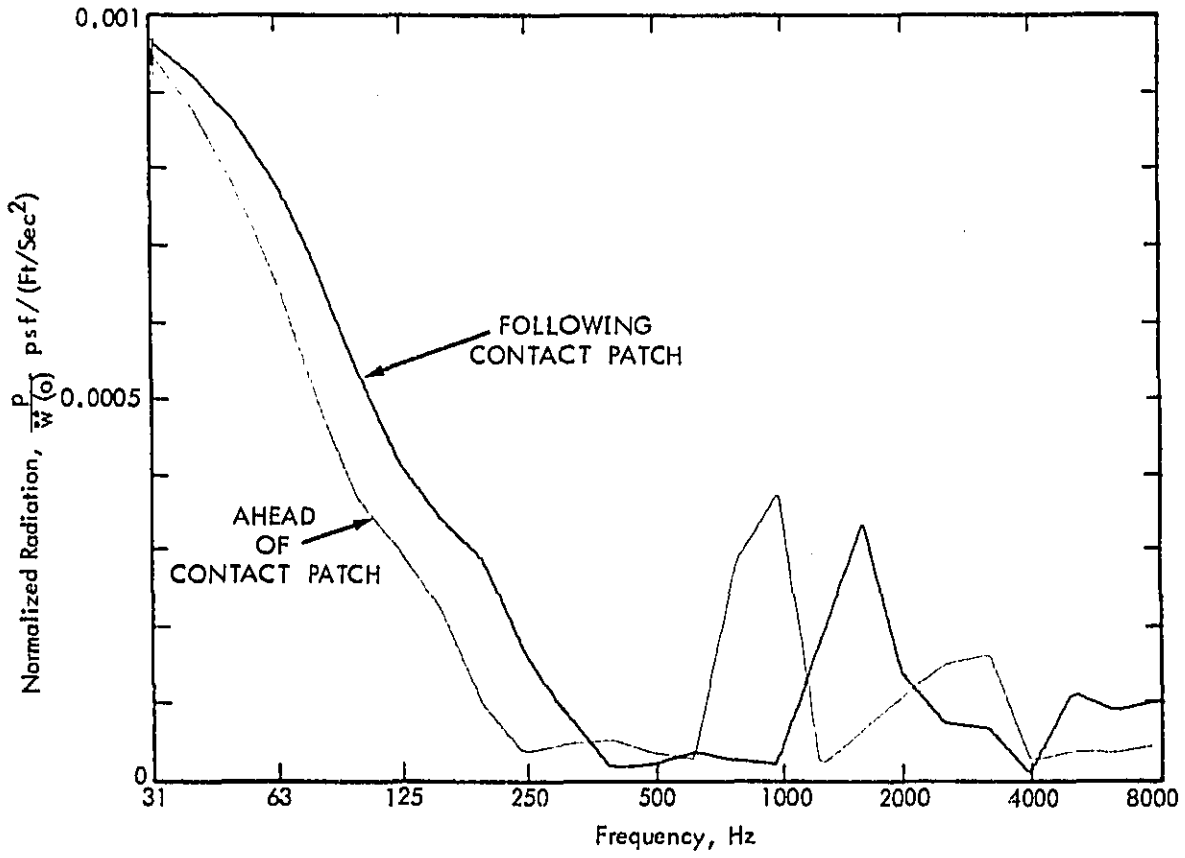
Figure 17. Sound Radiation From Tire A, 35 mph.
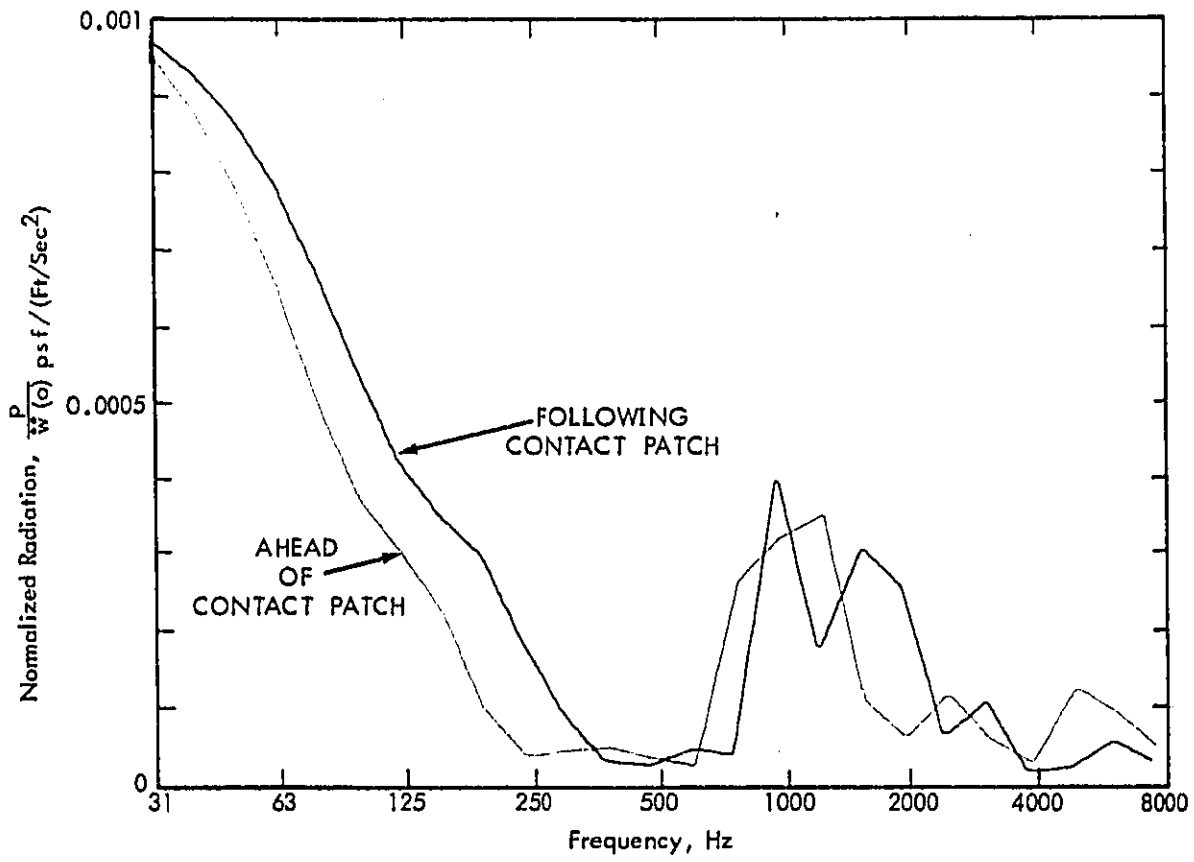
Figure 18. Sound Radiation From Tire B, 35 mph.

5.0 LOW NOISE DESIGNS

The noise models presented in Sections 2 through 4 provide a means of predicting noise due to air pumping and carcass vibration for a given tire design. Approaches to quiet design can be identified from trends in the noise models. This section discusses such low-noise design approaches. Included in the discussion are details not yet quantified in the models which must be studied in the experimental phase.

5.1 Effect of Carcass Design

The carcass has the following roles in noise emission:

(1) The stationary shape, and associated κ'', influence air pumping noise.

(2) The point source response $f(0)$ governs the transformation of contact force load into vibratory excitation.

(3) The vibrating tread belt area radiates sound.

The effect of (1) is quite clearly seen in Figure 13: increasing tread belt stiffness clearly reduces air pumping, as expected. It apparently has little effect on (2) and (3). While derivatives of f are influenced, the value of f itself does not change significantly with belt stiffness. The belt stiffness thus affects the tire shape in a way which influences air pumping (dependent on fourth derivative of shape) but does not affect carcass response and radiation (which depend only on lower derivatives of shape). Increasing belt stiffness thus appears to be a useful method of reducing air pumping, with no adverse effects on vibration noise.

A detail left out of f is the vertical compression of the tread rubber. The relation between ζ and z_s for pavement texture depends strongly on the vertical stiffness of the tread. Softening the tread should reduce pavement texture noise and noise associated with smaller tread elements, although the net impulse for larger elements would not change. Changing rubber compound is one approach, which, however, may not be practical because of the effect on durability. Another approach would be the addition of cuts and sipes which provide lateral expansion space when the tread is loaded. This approach can be experimentally studied by successively cutting a test tire. The effect should be strongest where pavement texture noise is dominant. Potential performance effects might be decreased durability due to small elements breaking off, and increased wet traction due to additional drainage.

5-1

5.2 Effect of Tread Design on Air Pumping

Referring to Equations (25) and (29), air pumping is directly related to basic void dimensions. Decreasing lateral width provides a direct reduction: this should be minimized as much as possible within the constraint of soft-surface traction. If a certain total void volume is required, this can be maintained by increasing l_v without changing total pitch l. Reducing tread pitch reduces air pumping per void, but increases the number of voids per unit time. Considering the noise from each void to act independently, the detected average sound pressure would vary as $\sqrt{l}$. Care must be taken when changing l_v or l not to adversely affect A', as discussed in Section 5.3 below.

The most dramatic reduction to air pumping can be obtained by slanting the voids. Figure 19 shows the effect of changing void angle. The noise reduction is substantial as angles are reduced from 90°. It should be noted that the trend shown in Figure 19 applies to the average angle; a zig-zag void which runs on average directly across the tire is not significantly different from a straight 90° void.

The calculation per void shown in Figure 19 applies equally to crossbar and rib patterns, as shown in Figure 20. Appropriate values of the geometric factor G in both cases, and flow blockage ϵ for rib grooves, must be applied. Two other factors must be considered:

- The angle, throw, and pitch of a zig-zag rib groove, as shown, are interrelated so as to have a continuous groove.

- The contributions from cross-grooves directly add, allowing for differences in time. The rib groove elements appear sequentially, with the effective value of ϵ decreasing for each element as the next moves into the contact patch.

The strong attenuation of pumping for each rib element implies that the effect of angle on rib air pumping is qualitatively complete in Figure 19. The effect of a full cross-groove pattern requires summation of the independent contributions.

Figure 21 shows a calculation similar to Figure 19, but for a sequence of five grooves. The result generally looks like a repetition of independent pulses. At 45°, however, the monopole signal vanishes. At this angle, the circumferential extent of each groove matches the tread pitch, and the positive and negative portions of the pulses cancel. There will still be air pumping noise, but in the form of dipoles with much lower levels.
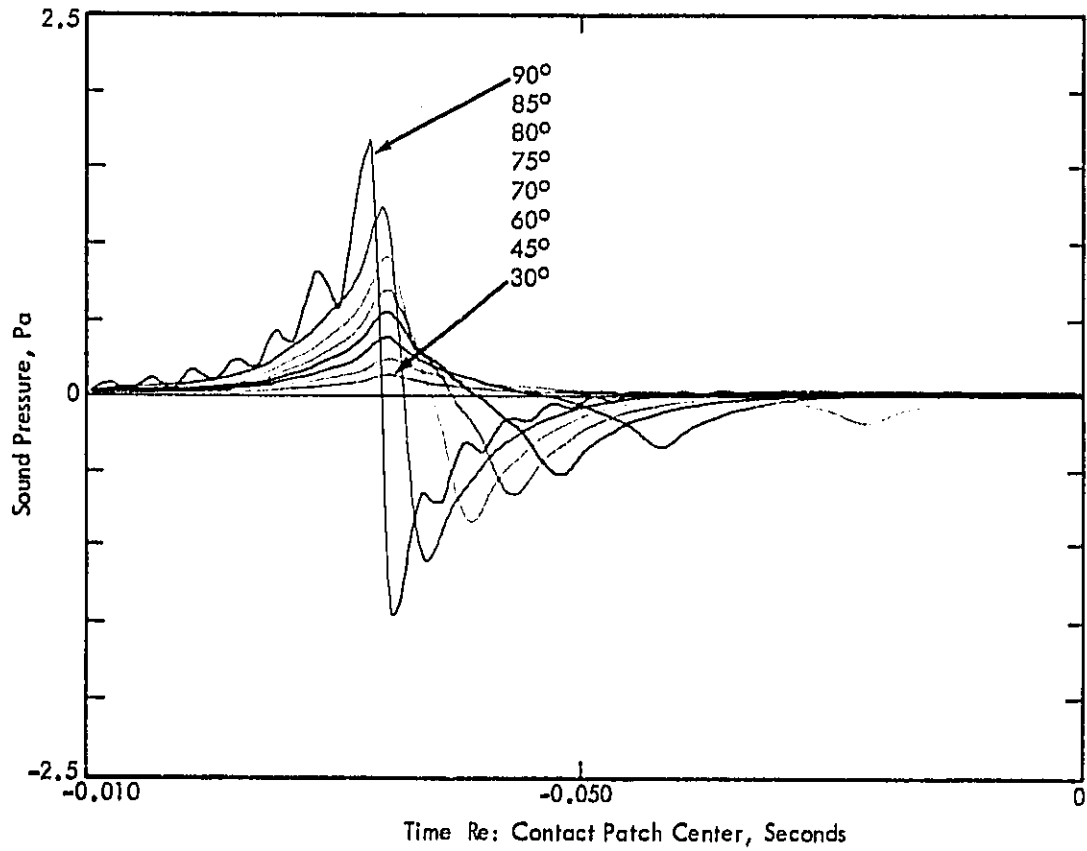
Figure 19. Calculated Air Pumping Per Groove As a Function of Groove Angle, Tire B.
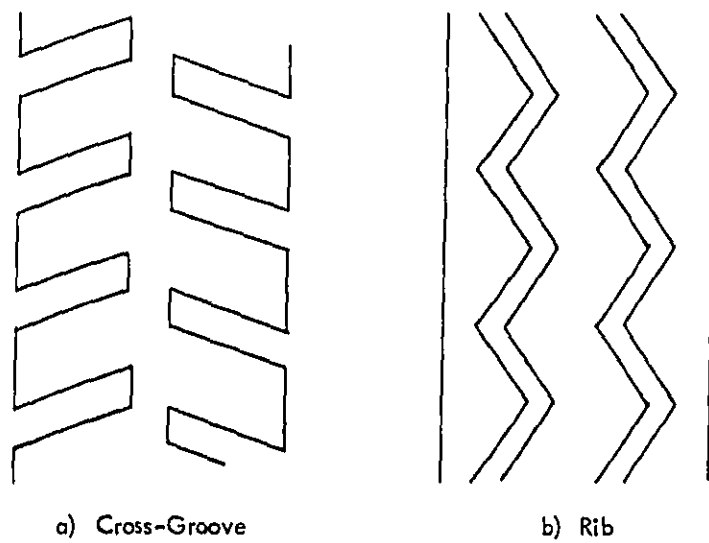
    a) Cross-Groove   b) Rib

Figure 20. Cross-Groove and Rib Tread Patterns.
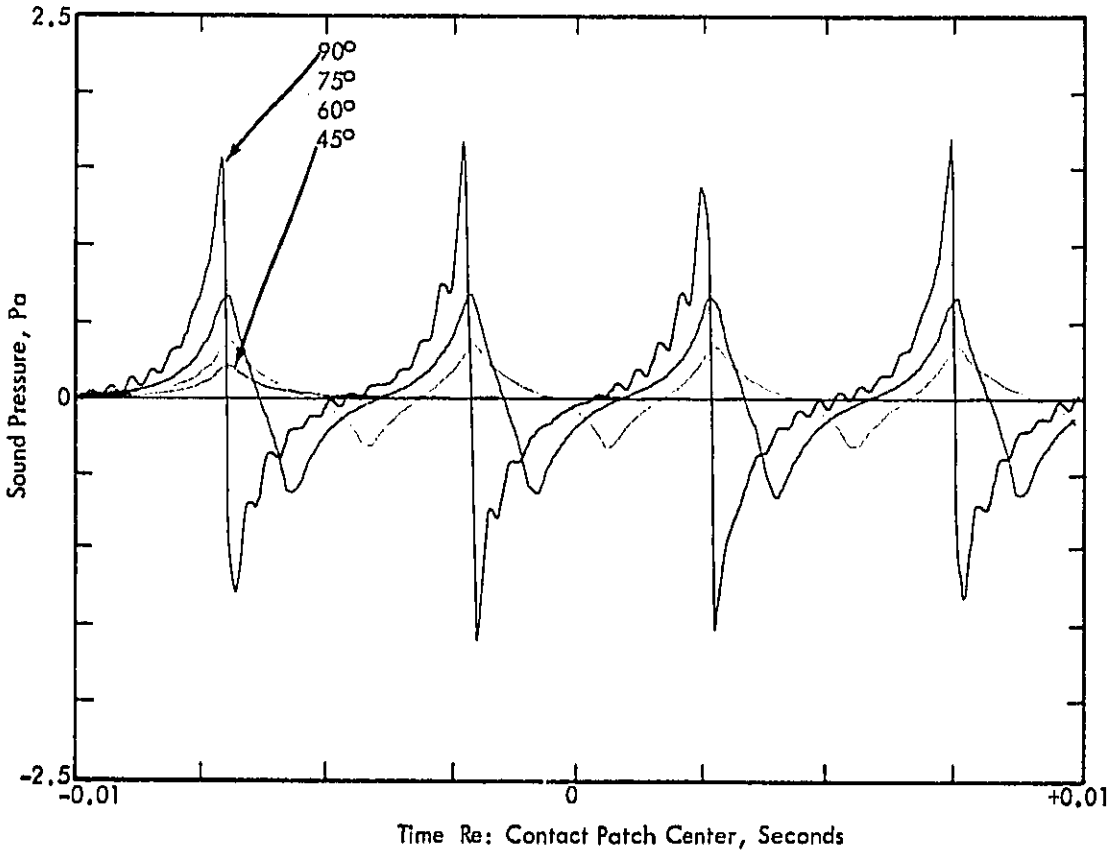
Figure 21. Calculated Air Pumping From a Sequence of Grooves as a Function of Groove Angle, Tire B.

Figure 21 shows that by proper spacing of voids, phase cancellation can minimize air pumping noise. This result depends strongly on the rather symmetric form of κ'' predicted by the carcass model, plus the various other idealizations included in the model. Pending experimental verification of these details, this is a potentially promising noise reduction approach. It would also be consistent with reducing A', the key to tread pattern vibration excitation.

5.3 Effect of Tread Design on Carcass Vibration

The key parameter in vibration excitation is A', as seen in Equation (45). For a typical zig-zag rib pattern as shown in Figure 20b, A' is a series of step functions. For a given tread throw (total lateral extent of groove), the impulse per element is constant. The obvious approach is to reduce tread throw, tending toward straight circumferential grooves. This is a trivial solution, however, and is not worth pursuing in the present program. Several more subtle approaches exist which may provide less of a compromise with tractive performance:

- A' is a combination of geometric area and lateral pressure distribution. Proper lateral placement of tread features may provide some noise minimization.

- Placing multi-element patterns so as to minimize the collective A' is important. Placing similar tread cycles 1/2 out of phase will achieve this; see the sketches in Figure 20. The phase cancellation cross-groove pattern discussed in Section 5.2 is consistent with this.

- The square wave A' associated with zig-zag grooves has a spectrum rich in harmonics. Rounding the corners would reduce higher frequency excitation, yet leave the basic tread pattern similar to its original design. The usefulness of this approach will depend on the net frequency content of the whole system.

- Fine detail with A' of opposite sign from that of the basic pattern could be employed. Lateral placement will be important for this approach.

5- 6

REFERENCES

1. Plotkin, K.J., "National Exposure to Highway Noise Through the Year 2000", Wyle Research Report WR 77-13, for the U.S. Environmental Protection Agency, July 1979.

2. Sharp, B.H., "A Survey of Truck Noise Levels and the Effect of Regulations", Wyle Research Report WR 74-8, for the U.S. Environmental Protection Agency, December 1974.

3. "Sound Level of Highway Truck Tires", SAE Recommended Practice J57a.

4. Leasure, W.A., "An Assessment of Tire Noise Reduction Options in the United States Today", paper presented at the International Tire Noise Conference, Stockholm, August 1979.

5. Timmons, F.E., "An Industry Viewpointing of Tire Sound Reduction and Measurement Methodology", Society of Automotive Engineers 762020, November 1976.

6. Nilsson, N.A., "Possible Methods of Reducing External Tire Noise", paper presented at the International Tire Noise Conference, Stockholm, August 1979.

7. Plotkin, K.J., Montroll, M.L., and Fuller, W.R., "A Study to Identify Advanced Methods of Reducing Tire Noise", Wyle Research Report WR 80-16, for the U.S. Environmental Protection Agency, April 1980.

8. Bohm, F., "Zur Statik und Dynamik Des Gurtelreifens", ATZ 69 (1967), 255-261. See Also "Mechanisms of the Belted Tire", Ingeniur-Archiv, XXXV, 1966.

9. Nilsson, N.A., "Generating Mechanisms of External Tire Noise", IFM Akustikbyran Report No. TR3.709.14, August 1976.

10. Eberhardt, A.C., "Investigations of the Truck Tire Vibration Sound Mechanisms", paper presented at the International Tire Noise Conference, Stockholm, August 1979.

11. Krapf, K.-G., "Vibration Measurements and Computation for the Radial Belted Tire", paper presented at the International Tire Noise Conference, Stockholm, August 1979.

12. Ginn, J.L., and Marlowe, R.L., "Road Contact Forces of Truck Tires Measured in the Laboratory", SAE Paper 670493, 1967.

13. Walter, J.D., Avgeropoulos, G.N., Janssen, M.L., and Potts, G.R., "Advances in Tire Composite Theory", Tire Science and Technology, TSTCA, Vol. 1, 210-250, May 1973.

14. Robecchi, E., and Amici, L., "Mechanics of the Inflated Tire", Tire Science and Technology, TSTCA, Vol. 1, 290-345, August 1973.

15. Robecchi, E., "Mechanics of the Pneumatic Tire. Part II. The Laminar Model Under Inflation and In Rotation", Tire Science and Technology, TSTCA, Vol. 1, 382-438, November 1973.

16. Brewer, H.K., "Prediction of Tire Stress and Deformation From Composite Theory", Tire Science and Technology, TSTCA, Vol. 1, 47-76, February 1973.

17. Posfalvi, O., "On the Mechanical Behavior of the Orthotropic Cord-Rubber Composite", Tire Science and Technology, TSTCA, Vol. 4, 219-232, November 1976.

18. DeWitt, M.A., engineering data on B.F. Goodrich heavy-duty radial truck tires. Private communication, May 1981.

19. Hayden, R.E., "Roadside Noise From the Interaction of a Rolling Tire With the Road Surface", Proceedings of the Purdue Noise Control Conference, July 1971.

20. Samuels, S.E., "Recent Australian Tyre/Road Noise Research", paper presented at the International Tire Noise Conference, Stockholm, August 1979.

21. Burroughs, C.B., and Bender, E.K., "Handbook of Tire Noise-Generating Mechanisms", BBN Report No. 3812, September 1978.

22. Thrasher, D.B., Miller, R.F., and Bauman, R.G., "Effect of Pavement Texture on Tire/Pavement Interaction Noise", SAE Paper 762011, November 1976.

23. Walker, J.C., "The Reduction of Noise by Applying Basic Design Principles to Roads and Tires", SAE Paper 762031, November 1976.

24. Morse, P.M., and Ingard, K.I., Theoretical Acoustics, McGraw-Hill, 1968.

25. Davis, P.J., and Rabinowitz, P., Methods of Numerical Integration, Academic Press, New York, 1975.